A Tale of Two Herbig Ae stars -MWC275 and AB Aurigae: Comprehensive Models for SED and Interferometry.

A. Tannirkulam[1], J. D. Monnier[1], T. J. Harries[2], R. Millan-Gabet[3], Z. Zhu[1], E. Pedretti[4], M. Ireland[5], P. Tuthill[5], T. ten Brummelaar[6], H. McAlister[6], C. Farrington[6], P. J. Goldfinger[6], J. Sturmann[6], L. Sturmann[6], N. Turner[6]

ABSTRACT

We present comprehensive models for the Herbig Ae stars MWC275 and AB Aur that aim to explain their spectral energy distribution (from UV to millimeter) and long baseline interferometry (from near-infrared to millimeter) simultaneously. Data from the literature, combined with new mid-infrared (MIR) interferometry from the Keck Segment Tilting Experiment, are modeled using an axisymmetric Monte Carlo radiative transfer code. Models in which most of the near-infrared (NIR) emission arises from a dust rim fail to fit the NIR spectral energy distribution (SED) and sub-milli-arcsecond NIR CHARA interferometry. Following recent work, we include an additional gas emission component with similar size scale to the dust rim, inside the sublimation radius, to fit the NIR SED and long-baseline NIR interferometry on MWC275 and AB Aur. In the absence of shielding of star light by gas, we show that the gas-dust transition region in these YSOs will have to contain highly refractory dust, sublimating at ∼1850K. Despite having nearly identical structure in the thermal NIR, the outer disks of MWC275 and AB Aur differ substantially. In contrast to the AB Aur disk, MWC275 lacks small grains in the disk atmosphere capable of producing significant 10-20 μm emission beyond ∼7AU, forcing the outer regions into the "shadow" of the inner disk.

Subject headings: young stellar objects — circumstellar disks — radiative transfer — Monte Carlo codes— dust sublimation — grain evolution — interferometry

[1]atannirk@umich.edu: University of Michigan, Astronomy Dept, 500 Church Street, 1017 Dennison Bldg, Ann Arbor, MI 48109-1042, USA

[2]University of Exeter, School of Physics, Stocker Road, Exeter, EX4 4QL, UK

[3]Michelson Science Center, Pasadena, CA, USA

[4]University of St. Andrews, Scotland, UK

[5]School of Physics, Sydney University, N. S. W. 2006, Australia

[6]CHARA, Georgia State University, Atlanta, GA, USA

1. Introduction

Herbig Ae (HAe) stars are pre-main-sequence stars of intermediate mass (1.5-3 solar masses). They exhibit a robust excess in emission over stellar photospheric values from near-infrared (NIR) to the millimeter (mm) wavelengths. This excess is now attributed to the passive reprocessing of stellar light by dust in the circumstellar environment (Tuthill et al. 2001; Natta et al. 2001; Dullemond et al. 2001). The geometry of the circumstellar environment of HAe stars has been actively debated in the astronomy community over the last two decades. Some of the early workers in this field (Hillenbrand et al. 1992) showed that spectral energy distribution (SED) of HAe stars could be explained by emission from circumstellar matter in disk-like geometry. Others (Miroshnichenko et al. 1997) argued that the emission could also arise from dust in a spherical geometry around the star, proving the inadequacy of SED modeling alone in uniquely fixing the geometry of the circumstellar matter. The first observational evidence in favor of a disk geometry came from millimeter (mm) interferometry in the form of asymmetries detected (Mannings & Sargent 1997) in the mm images. Asymmetries in the NIR emission were also detected by the Palomar Test-Bed Interferometer (Eisner et al. 2003, 2004), settling the debate in support of a disk geometry for circumstellar material in Herbig Ae stars.

Most interferometric studies of HAe stars have relied on simple geometric models (Mannings & Sargent 1997; Millan-Gabet et al. 1999, 2001; Eisner et al. 2003, 2004; Monnier et al. 2005) that explain the emission geometry of the system in only narrow wavelength ranges. This method, albeit extremely useful in elucidating some of the morphology details, is not adequate for exploring the interdependency in structure of the inner and outer parts of the disk. A number of studies (Dullemond et al. 2001; Dullemond & Dominik 2004; van Boekel et al. 2005b) have shown that the structure of the inner disk at fractions of an AU scale clearly affects the structure of the outer disk. A complete understanding of the circumstellar disk structure in HAe stars therefore requires models that simultaneously explain the SED and interferometry over a large wavelength range. Such models have begun to appear in the literature only recently (Pontoppidan et al. 2007; Kraus et al. 2008).

In this paper, we develop comprehensive disk models to explain the SED and interferometry of the HAe stars MWC275 and AB Aur. MWC275 and AB Aur are prototype pre-main-sequence stars of similar ages and spectral type with extensive circumstellar disks. Due to the availability of photometric and interferometric data over a large wavelength range, MWC275 and AB Aur are ideal candidates for testing disk models for YSOs. The extent of their circumstellar-dust disks was first measured by Mannings & Sargent (1997) to be several 100AU using the Owens Valley Radio Observatory (OWRO). Natta et al. (2004) resolved the MWC275 disk in the mm and reported a de-convolved, projected dust-disk size of

300AU×180AU. More recently, Isella et al. (2007) analyzed IRAM, SMA and VLA continuum and ^{12}CO, ^{13}COand ^{18}CO line data constraining the gas-disk radius to be 540AU with the gas in Keplerian rotation around the central star. Scattered light studies of MWC275 (Grady et al. 2000) and AB Aur (Grady et al. 1999; Oppenheimer et al. 2008) show the presence of arcs and rings in the circumstellar disk. Corder et al. (2005) resolved the AB Aur CO disk radius to be ∼600AU, finding strong evidence for Keplerian rotation for the bulk of the disk. Corder et al. (2005) and Lin et al. (2006) detected spiral arms in CO emission with radii of ∼150AU, while Fukagawa et al. (2004) detected similar structure in Subaru H-band scattered light images. AB Aur also has substantial envelope material on scales larger then 600 AU (Grady et al. 1999; Semenov et al. 2005; Corder et al. 2005; Lin et al. 2006).

MIR emission probes the giant planet formation region in circumstellar disks (Calvet et al. 1992; Chiang & Goldreich 1997; Dullemond et al. 2001) with the emission arising from warm dust (T > 150K). Meeus et al. (2001) and van Boekel et al. (2005) used the 10μm MIR silicate emission feature from MWC275 and AB Aur to show that dust grains in these systems had grown larger than the typical interstellar medium grain sizes. Mariñas et al. (2006) imaged AB Aur at 11.7μm and found the emission FWHM size to be 17±4 AU consistent with the flared disk models of Dullemond & Dominik (2004). In this paper, we present new 10μm measurements of AB Aur and MWC275 with the Keck Segment Tilting Experiment (Monnier et al. 2004, described in §2). In contrast to AB Aur, the MWC275 disk is unresolved by the Segment Tilting Experiment (maximum baseline of 10m), requiring the VLT Interferometer (100m baseline) to probe to its MIR structure (Leinert et al. 2004). These observations suggest that MWC275 disk differs considerably from AB Aur and we present a detailed comparison of the two disk structures in the discussion (§6).

Thermal NIR emission probes hot regions (typically the inner AU) of the disk with temperatures greater than 700K. The NIR disks of MWC275 and AB Aur were first resolved with IOTA by Millan-Gabet et al. (1999, 2001) and subsequently observed at higher resolution with PTI (Eisner et al. 2004), Keck Interferometer (Monnier et al. 2005) and the CHARA interferometer array (Tannirkulam et al. 2008). In Tannirkulam et al. (2008, hereafter T08) we showed that inner-disk models in which majority of the K-band emission arises in a dust rim (Dullemond et al. 2001; Isella & Natta 2005; Tannirkulam et al. 2007) fail to fit the CHARA data at milli-arcsecond resolution. We also demonstrated that the presence of additional NIR emission (presumably from hot gas) inside the dust destruction radius can help explain the CHARA data and the NIR SED. First calculations for the effects of gas on rim structure (Muzerolle et al. 2004) showed that for plausible disk parameters, presence of gas does not modify dust-rim geometry significantly. Besides a poorly understood interferometric visibility profile, MWC275 also displays as yet ill-understood NIR and MIR SED time variability (Sitko et al. 2008) which has been interpreted as variations of the inner

disk structure. In §4 and §5 we present a detailed analysis of the NIR visibility and SED for MWC275 and AB Aur, placing constraints on the wavelength dependence of the opacity source inside the dust destruction radius.

In this study, we focus on (i) explaining the inner-disk structure and discuss important open problems and (ii) modeling the MIR emission morphology of the disks and the shape of the MIR spectrum. The paper is organized into 7 sections with §2 detailing the observations. §3 explains the disk model and the modeling strategy. §4 and §5 analyze MWC275 and AB Aur SED and visibilities in relation to the disk models. We present a discussion on our results and our conclusions in §6 and §7 respectively.

2. New Observations and Literature Data

The properties of the circumstellar disks in MWC275 and AB Aur have been constrained using IR and mm interferometry and SED. We include new NIR interferometry from the CHARA array, MIR interferometry from the Keck Segment Tilting Experiment and mm interferometry from the literature in our analysis. Optical and NIR photometry obtained at the MDM Observatories, and mid and far-infrared data from ISO are also included to constrain model SED. We describe the data in detail in the following paragraphs.

K-band (central wavelength of 2.13μm, $\Delta\lambda$ 0.3μm) interferometry on MWC275 and AB Aur, first presented in T08, was obtained using the CHARA array with the 2-beam CHARA "Classic" combiner at the back end (ten Brummelaar et al. 2005). The targets were observed with multiple baselines of CHARA at a variety of orientations in 8 runs between June 2004 and June 2007. The longest baseline observation for MWC275 was 325m (resolution [1] of 0.67 milli-arcseconds) and 320m (resolution of 0.68 milli-arcseconds) for AB Aur. The data were reduced using standard CHARA reduction software (ten Brummelaar et al. 2005) and these results were cross-checked with an independent code developed at University of Michigan. HD164031 , HD166295 and HD156365 with uniform-disk (UD) diameters of 0.83± 0.08 mas, 1.274±0.018 mas and 0.44±0.06 mas (Merand et al. 2005, and getCal - http://mscweb.ipac.caltech.edu/gcWeb/gcWeb.jsp) were used as calibrators for MWC275. AB Aur visibilities were calibrated with HD29645 (UD diameter=0.54±0.07 mas, getCal) and HD31233 (UD diameter=0.76±0.13 mas, getCal). During the reduction procedure the flux ratios between the two interferometer telescopes were carefully monitored for the source and the calibrators. Data points having a flux ratio variation greater than 10% of the mean,

---

[1]Resolution is defined as $\frac{\lambda}{2D}$, where λ is wavelength of observation and D is the interferometer baseline length.

indicating large changes in instrument alignment, were discarded. Three MWC275 data points were removed by this criterion. The procedure was adopted to minimize calibration errors caused by differences in beam overlap in the source and calibrator. The relative visibility errors which include calibration errors, statistics and uncertainties in calibrator size, are at the $\sim 6\%$ level, typical for CHARA Classic. In T08, we had shown the reduced data briefly in the form of visibility interferometric-baseline plots. Here we present the complete observing logs with the uv coverage (see Figs 1 and 2) and the calibrated visibilities listed in Tables 1 and 2. NIR interferometry from IOTA (Monnier et al. 2006), PTI (Eisner et al. 2003, 2004) and the Keck Interferometer (Monnier et al. 2005) have also been included to constrain the models.

MW275 and AB Aur were observed with the Keck Segment Tilting Experiment (Monnier et al. 2004) to study their MIR emission morphology. Four subsets of Keck primary mirror segments were repointed and rephased so as to achieve four separate sparse aperture Fizeau interferometers, each with a separate pointing origin on the LWS detector (Jones & Puetter 1993). The details of the experiment and the data reduction procedure are provided in Monnier et al. (2004) and Monnier et al. (2008, in prep). The calibrated data are listed in Table 3. In addition to the Keck Segment Tilting data, we also include MWC275 MIR intereferometry from VLTI-MIDI (Leinert et al. 2004) in our analysis.

Millimeter interferometry from Mannings & Sargent (1997), Natta et al. (2004), Semenov et al. (2005), Lin et al. (2006) and Isella et al. (2007) are used to constrain the circumstellar disk masses and disk sizes and surface density profile. In conjunction with the interferometry, the shape of the mm SED provides information on sizes of the dust grains in the bulk of the circumstellar disks.

To constrain the SED computed from radiative transfer models we obtained optical and NIR photometry on MWC275 and AB Aur with the MDM 2.4m telescope at Kitt Peak. Due to the high brightness of our targets, we defocussed the telescope during observations to avoid camera saturation. After bias correction, flat fielding, and background subtraction, the reduced images were used to obtain source counts using ATV - an aperture photometry code (Barth 2001). Targets were calibrated using Landoldt standards (Landolt 1983). The calibrated UBVRIJHK photometry are listed in Tables 10 and 11 in the Appendix. We also include photometry for a number of other YSOs that we observed. NIR photometry from Sitko et al. (2008) , mid and far-IR SED from Meeus et al. (2001) and mm fluxes (Mannings & Sargent 1997; Natta et al. 2004; Semenov et al. 2005; Lin et al. 2006) were also used in the model analysis. van Boekel et al. (2005) modeled the $10\mu m$ spectra of a large sample of Herbig Ae stars and derived the mineralogy and typical grain sizes responsible for the emission. We use results from van Boekel et al. (2005) for fixing the composition of dust

grains in the atmosphere of the MWC275 and AB Aur disks.

A compilation of stellar properties and circumstellar disk properties extracted from the literature is listed in Tables 4, 5, 6 and 7.

3. Circumstellar Disk Modeling

The circumstellar material around MWC275 and AB Aur is modeled as a passive dust disk reprocessing stellar radiation (Dullemond et al. 2001). The disk is in thermal and hydrostatic equilibrium and can be divided into 3 distinct regions (Fig 3) -

- **Curved Inner Rim** Sufficiently close to the star (distance depends on stellar luminosity and dust sublimation temperatures), dust in the circumstellar disk reaches sublimation temperatures and evaporates. Inside of the evaporation radius, the disk is optically thin. The truncated dust disk is frontally illuminated by the star and forms a 'rim' whose shape depends sensitively on dust properties (Isella & Natta 2005; Tannirkulam et al. 2007). The rim puffs up, traps a significant fraction of stellar photons and re-radiates predominantly in the NIR (Dullemond et al. 2001).

- **Shadow Region** The inner rim casts a geometric shadow on the region behind it (Dullemond et al. 2001; Dullemond & Dominik 2004), preventing it from receiving direct star light. The shadow is heated by scattered photons from the rim edge and through diffusion. The size of the shadow depends on the rim geometry, mass of dust in the outer disk and dust grain properties in the outer disk.

- **Flared Disk** If sufficient dust is present in the outer disk, the disk eventually emerges from the shadow and "flares". The flared disk emits radiation in the MIR and longer wavelengths.

Details of the modeling procedure and comparison to data are described below.

3.1. The Monte Carlo Transfer Code - TORUS

The calculations in this paper were performed using the TORUS Monte-Carlo radiative-transfer code (Harries 2000; Harries et al. 2004; Kurosawa et al. 2004; Tannirkulam et al. 2007). Radiative equilibrium is computed using Lucy's (Lucy 1999) algorithm on a two-dimensional, cylindrical adaptive-mesh grid. The initial density structure for the disk calculations is based on the canonical description of the α-disk developed by Shakura & Sunyaev

(1973), viz

$$\rho(r, z) = \rho_0 \left(\frac{r}{r_0}\right)^{-\alpha} \exp\left[-\frac{1}{2}\frac{z^2}{h(r)^2}\right] \tag{1}$$

where r is the radial distance in the mid-plane, r_0 is some characteristic radius, z is the distance perpendicular to the mid-plane, and $h(r)$ is the scaleheight, given by

$$h(r) = h_0 \left(\frac{r}{r_0}\right)^{\beta} \tag{2}$$

with parameters of $\alpha = 2.125$ and $\beta = 1.125$, giving a radial dependence of the surface density of $\Sigma(r) \propto r^{-1.0}$. Once the temperature (we assume that the disk is in local thermodynamic equilibrium passively heated by the star, and gas and dust are thermally coupled) and dust sublimation (see next paragraph) structures have converged using the Lucy algorithm, the vertical disk structure is modified via the equation of hydrostatic equilibrium following a similar algorithm to that detailed by Walker et al. (2004). A self-consistent calculation for dust sublimation and disk temperature followed by a hydrostatic equilibrium calculation is repeated until the disk density structure has converged. Convergence is typically achieved in four iterations. Images and SEDs are subsequently calculated using a separate Monte Carlo algorithm based on the dust emissivities and opacities (Harries 2000).

The shape of the dust evaporation front is computed following Tannirkulam et al. (2007). The dust content is first reduced to a very low value in the computational grid for the circumstellar disk, to make each of the grid cells optically thin. Stellar photons then propagate through the disk and the temperature of grid cells is determined. Dust is added to cells that are cooler (see eqn 3 for sublimation temperature parameterization) than the sublimation temperature in small steps of τ. The step size is a τ of 10^{-3} (computed at 5500Å) for the first five dust growth steps. The step size is then increased logarithmically, first to 10^{-2}, then to 10^{-1} and so on until a 100:1 gas to dust ratio is reached in each grid cell. The grid cell temperatures are recomputed after every dust growth step and the process is repeated until the shape of the dust sublimation region converges.

We use Kurucz (Kurucz 1970) stellar atmosphere models as input spectra for the stars. We consider a mixture of 0.1,1.3 and 50 micron warm silicates (Ossenkopf et al. 1992) and power-law opacity mm grains (Mannings & Sargent 1997; Natta et al. 2004) to model the opacity in the disk. The micron and sub-micron grain mixture is based on work by Meeus et al. (2001) and van Boekel et al. (2005). To keep the analysis simple, the grain species are assumed to be well mixed with gas following a delta function size distribution. Dust scattering is not included in the models. Scattering does not seem to have significant impact on disk structure and interpretation of infrared interferometry for HAe stars (Dullemond & Natta 2003; Pinte et al. 2008).

During the course of our modeling and as outlined in Tannirkulam et al. (2008), we realized that an additional emission component (Fig 3), which we argue to be gas, is needed inside the dust destruction radius to explain the NIR SED and interferometry of MWC275 and AB Aur (see section 4.1.2 for discussion on gas opacity). This additional component is not treated self consistently in our modeling and is added after the dust-opacity-dominated circumstellar-disk model converges in structure. Calculations by Muzerolle et al. (2004) have shown that for parameters suitable to MWC275 and AB Aur, gas does not significantly alter the structure of the dust rim, justifying our simple treatment for the NIR emission geometry.

In sections 4.1.1 and 5.1, we demonstrate that the NIR emitting region in MWC275 and AB Aur has a radius of ∼0.2AU. Furthermore, long-baseline interferometry beyond the first visibility minimum constrains the gas and dust emission to be on similar length scales (Fig 7). The two statements together imply that in the absence of shielding of the evaporation front by gas, the mid-plane sublimation temperature in the dust rim is ∼1850K (see section 4.1.1).

3.2. Comprehensive models for SED and Interferometry

To fit the SED and visibilities of MWC275 and AB Aur we adopted the following algorithm: First, we computed models for the dust evaporation front as described in §3.1. The inner edge of the dust disk is assumed to be dominated by grains larger than 1 micron (Tuthill et al. 2001; Isella et al. 2006) and the evaporation front shape is set by the density dependence of dust sublimation temperatures (Isella & Natta 2005; Tannirkulam et al. 2007). The K-band visibilities are computed for the model and compared with data. The normalization of the dust evaporation law is then adjusted so that the model visibilities fit the visibility data before the first visibility minimum. These models fail to fit the visibility beyond the minimum and do not have sufficient emission to explain the observed NIR SED. Therefore an additional emission component has been added inside the dust sublimation radius to reconcile the model with the visibility data and NIR SED.

With the inner-rim parameters fixed, we next focus on MIR and the mm disk. Millimeter interferometry results from the literature are used to fix disk masses and sizes. The majority of the dust mass is placed in mm sized grains with a power-law opacity function (Natta et al. 2004). A small fraction (∼10%) of the dust mass is in micron and sub-micron (small) grains with their relative mass fractions based on literature results (Meeus et al. 2001; van Boekel et al. 2005). The physical extent of small grains is constrained with MIR imaging and interferometry. The model is then allowed to run to convergence. The model SED is compared with MIR and far-infrared data, the mass of the small grain population is then adjusted and models are recomputed until a good fit to the MIR and far-infrared SED

is obtained.

The MIR visibilities are computed for the SED-converged model and compared with the data and the spatial distribution of the small grain component is adjusted until model visibilities match with data. The only free parameters in our models are the absolute masses of the small grains, mass of the 50μm silicate grain and their spatial distribution. Each of the models is computationally expensive. To achieve fast convergence, the parameter space was varied by hand, until a good fit was found for the observable quantities.

4.   MWC275: Analysis

MWC275 is a Herbig Ae star (refer to Table 4 for basic properties and photometry) with a total luminosity of 36L$_\odot$. The large stellar luminosity, coupled with the fact that the mass accretion rate is $\leq 10^{-7}$M$_\odot$/year (Garcia Lopez et al. 2006) allows us to ignore accretion heating and model the MWC275 circumstellar disk as a passive disk, reprocessing stellar radiation (Chiang & Goldreich 1997; Dullemond et al. 2001). For our models, we choose the MWC275 disk mass to be between 0.05-0.1 M$_\odot$ (Natta et al. 2004) and a surface density profile that varies radially as r^{-1} (Isella et al. 2007). The disk outer edge is truncated at 200AU and bulk ($\sim$80%) of the dust mass is assumed to reside in mm grains having an opacity with a wavelength dependence of λ^{-1} at long wavelengths. Here, we describe in detail our modeling results for the NIR and MIR morphology of MWC275.

4.1.   The Thermal NIR Disk

4.1.1.   Visibilities

Like many other Herbig Ae stars, MWC275 shows a strong NIR excess over stellar photospheric values (Hillenbrand et al. 1992). This excess has been traditionally interpreted in terms of the dust disk being truncated by sublimation and forming a 'rim'. The rim intercepts stellar photons, re-radiating predominantly in the NIR (Dullemond et al. 2001; Isella & Natta 2005; Tannirkulam et al. 2007). However, in T08 we had conclusively shown that models in which all of the NIR excess arises from dust rims alone cannot explain the CHARA interferometry data on MWC275. Our arguments in T08 were necessarily brief. We present a more elaborate analysis in this section.

MWC275 observations allow us to clearly detect the asymmetry of the MWC275 disk (see Appendix A.2), as having inclination=48°±2°, PA=136°±2°, consistent with the incli-

nation of 51^{+11}_{-9} degrees, PA of $139^o \pm 15^o$ determined in Wassell et al. (2006) and inclination of $46^o \pm 4^o$, PA of $128^o \pm 4^o$ determined in Isella et al. (2007). The complete visibility data along each of the baselines are presented in Fig 4. Following T08, we show the data in a concise manner in Fig 5 using the notion of an "effective baseline" -

$$B_{eff} = B_{projected}\sqrt{\cos^2(\theta) + \cos^2(\phi)\sin^2(\theta)}$$

where θ is the angle between the uv vector for the observation and the major axis of the disk and ϕ is the inclination of the disk. Under the flat disk assumption, the effective baseline correctly accounts for the change in resolution due to the disk inclination and PA (the geometry of thick disks is represented only approximately with optical depth effects and 3-D geometry of thick disks not being taken into account), allowing us to plot the visibility measurements as a function of one coordinate, simplifying presentation and analysis.

We attempt at fitting the visibilities with a curved inner-rim model (the "standard" model) where the rim curvature (variation in cylindrical radius between rim midplane and the atmosphere) is set by the density dependence of dust sublimation temperatures, taken from Pollack et al. (1994). In this model, silicate grains sublimate at a higher temperature compared to other grains and hence fix the rim location. The rim is assumed to be composed of 1.3μm grains, as larger grains do not affect the rim shape and location significantly (Isella & Natta 2005), at the same time making numerical convergence slower due to strong back-warming effects (Isella & Natta 2005; Tannirkulam et al. 2007). For silicate dust, the evaporation temperature T_{evp} can be parameterized as

$$T_{\mathrm{evp}} = G\left[\frac{\rho_{\mathrm{gas}}(r,z)}{1\mathrm{g\ cm}^{-3}}\right]^\gamma \tag{3}$$

where $G = 2000\,\mathrm{K}$, $\gamma = 1.95 \times 10^{-2}$ and ρ_{gas} is the density of gas in $\mathrm{g\,cm}^{-3}$ (see IN05 eq. [16]). This parameterization, derived from a fit to sublimation temperatures recorded in the laboratory (Pollack et al. 1994), produces a dust rim with an inner edge at 0.36 AU (Fig 6a). The rim radius is too large to fit even the relatively short baseline visibility data from IOTA (Figs 4 and 5). In order to fit the data before the first visibility minimum, we had to increase the T_{evp} normalization-G by $\sim$30% from 2000K to 2600K. This increases the sublimation temperature at the base of the rim from $\sim$1350K to $\sim$1800K. Fig 6b shows the synthetic K-band image for the rim with the increased normalization. The dashed line in Fig 4 traces the visibility for this model and provides a good fit to the short baseline (< 100m) data.

However, as seen in Figs 4 and 5, rim models which are sharply truncated due to dust sublimation and produce all of the NIR excess, fail to fit observations beyond the first visibility minimum. These models display bounces in visibility at long baselines (not seen in the data) because of the presence of sharp ring-like features with high spatial frequency

components in the corresponding images, even for the smoothest rims physically plausible. In T08, we showed that the presence of a smooth emission component inside the dust destruction radius (Fig 6c) providing 56% of the total K band emission helps fit the data well (solid line in Figs 4 and 5). The NIR visibility data cannot constrain the surface brightness profile of the smooth emission component (we have adopted a constant surface brightness profile - a Uniform Disk for simplicity), but can constrain the size scale of the emission fairly robustly. Fig 7 shows a series of visibility curves where the smooth emission component is fixed to be 56% of the total emission and the radius of the Uniform Disk component is decreased by 15% successively from the initial radius of 0.23AU radius. The model image is then rescaled to maintain a good visibility fit at baselines shorter than 100m. It can be seen in Fig 7 that for Uniform Disk (UD) radii smaller than 0.19AU, the model visibilities begin to deviate significantly from the observations. Thus, the CHARA data constrains the smooth emission component to be on the same length scale as the dust sublimation rim filling the region between the disk and the central star.

4.1.2. SED

Fig 8 shows the NIR SED for MWC275. Besides failing to explain the NIR interferometry, the standard model also fails at producing sufficient NIR emission to explain the MWC275 SED even in its 'low' state. In T08, we had shown that binarity and source variability cannot account for the discrepancy between the standard model and data. We had argued that the presence of smooth emission inside the dust destruction radius can help explain the NIR visibility and account for the "missing" NIR flux in standard models. Opacity candidates for the smooth emission component are: (1) a dusty halo around the stars (Vinkovic et al. 2006a) and (2) gas inside the evaporation front. However, to fit the visibility data, the halo emission would have to be closer to the star than the dust destruction radius in the disk. This would require even higher dust-sublimation temperatures than the ~ 1850K we are adopting.

The most plausible physical mechanism for the smooth emission is hot gas. The required emission levels to explain the long-baseline K-band visibility data can be obtained with optically thin gas ($\tau \sim 0.15$) with a temperature range of 2000K-3000K (Muzerolle et al. 2004; Eisner et al. 2007a; Eisner 2007b). Assuming that the gas has sufficient opacity to produce the difference in flux between the standard model and the observed photometry, we can place limits on the wavelength dependence of gas opacity. Fig 9 plots limits on the gas opacity (normalized at K band) such that flux from the gas component + the standard model falls within 10% of the observed photometry (we have assumed that gas does not

significantly alter the geometry of the dust rim). In the next 2 paragraphs we compare theoretical gas-opacity curves with our empirically derived opacity from SED.

Fig. 9 shows the wavelength dependence of molecular (Ferguson et al. 2005; Zhu et al. 2007) and free-free+free-bound (henceforth FF-BF) opacity, both good candidates for the gas emission (refer T08). At 5000K, FF-BF opacity (Ferguson et al. 2005) agrees well with the derived opacity at long wavelengths but overshoots limits shortward of 2μm. At temperatures greater than 8000K , FF-BF opacities rise quickly with wavelength producing excessive mid-infrared light.

Theoretical molecular opacities compare fairly with empirical derivation between 1μm and 4μm. Beyond 4μm , theoretical molecular opacities rise rapidly with wavelength. However, the observed SED can be matched with models only if the gas opacity is flat between 4μm and 9μm. Also at 2000K and 2500K, strong opacity bands of CO and water vapor are present at 2.5μm and 5μm respectively, which have not been observed in MWC275. This suggests that if molecules were contributing to the bulk of NIR opacity, then some of the species providing opacity between 4-8 μm in Ferguson et al. (2005) and Zhu et al. (2007) are being destroyed in the vicinity of Herbig Ae star MWC275. We note that FF-BF opacities seem to better fit the empirically derived values than molecular opacity.

Sitko et al. (2008) have obtained fairly dense time coverage on the NIR and MIR SED of MWC275. The NIR SED shows variability at the 20% level. During the same period, the flux in the visible shows no detectable change, indicating that that stellar luminosity remained fairly constant. Sitko et al. (2008) interpret their observations as variations in the structure of the thermal NIR disk. A variation in the NIR morphology of MWC275 was also detected in the interferometry. The NIR disk size deduced from the Keck Interferometer data (April 2003 epoch, Figs 4 and 5) is ∼20% larger than the size obtained with the CHARA data (June 2004-Aug 2006 epochs). The size determined from the S2W1 June2007 data also differs at the ∼25% level from the size obtained from earlier CHARA epochs. These variations are poorly understood and could be caused by changes in size/geometry, mass accretion rate and gas content in the inner disk. More evidence for MWC275 variability was recently reported by Wisniewski et al. (2008), who found changes in scattered light intensity between 1998 and 2003-2004.

4.2. MIR SED and Emission Morphology

van Boekel et al. (2005) analyzed the MIR SED (Fig 10) of MWC275 in detail and showed that the SED could be reproduced well with a grain mixture of 1.5μm and 0.1μm

silicates with mass ratio of 4:1. We use results from van Boekel et al. (2005) in fixing the small grain composition in our disk models.

As seen in Fig 10, the MWC275 SED falls sharply between 20μm and 30μm. This drop and the 10μm silicate feature can be simultaneously reproduced only if the mass fraction of the small grain dust component relative to gas beyond 7AU is less than 20% of the mass fraction inside of 7AU. If the small grain component is allowed to exist beyond 7AU, then the model far-infrared spectrum becomes much stronger than observed SED. Fig 10 shows a TORUS model SED that fits the MIR and longer wavelength spectrum of MWC275 well. In this model, 40% of the 8μm emission arises from the dust rim, with the rim contribution declining to $\sim$20% at 13μm. This model also fits the MIDI-VLTI MIR visibilities (Leinert et al. 2004) and reproduces the 0.8±0.1AU 11μm FWHM minor-axis size of MWC275 (Fig 11), naturally explaining why MWC275 is unresolved by the Keck Segment Tilting Experiment. The quality of the SED and visibility fit in the 8-15μm region is only moderate, probably due to the simple dust composition and distribution that we have assumed in the model. The initial model setup has been chosen to reproduce MWC275 mm-interferometry.

Table 8 lists disk parameters for the MWC275 model and Fig 12 shows the radial distribution of the small grain fractions. The mid-plane temperature profile and the "flaring" geometry of the disk surface are shown in Fig 13. The dust rim "shadows" (Dullemond et al. 2001; Dullemond & Dominik 2004) the region of the disk between 0.3 and 1AU beyond which the disk begins to flare. The τ=1 surface drops down in scale height steeply after 6.5AU where the small grain fraction reduces sharply. Our conclusions on dust-grain distribution in the MWC275 disk are consistent with that of Sitko et al. (2008).

5. AB Aur: Analysis

AB Aur is a Herbig Ae star (refer to Table 5 for basic properties and photometry) with a total luminosity of 47L$_\odot$ (Isella et al. 2006). As in the case of MWC275, AB Aur's large stellar luminosity dominates the circumstellar disk's energy budget (Garcia Lopez et al. 2006, accretion rates $\leq 10^{-7}$M$_\odot$/year). This allows us to ignore accretion heating and model the AB Aur circumstellar disk as a passive disk, reprocessing stellar radiation (Chiang & Goldreich 1997; Dullemond et al. 2001). For our models, we choose the AB Aur disk mass to be between 0.007-0.013 M$_\odot$ (Lin et al. 2006) and a surface density profile that falls radially as r^{-1} (Corder et al. 2005). The disk outer edge is truncated at 300AU and the bulk ($\sim$80%) of the dust mass is assumed to reside in mm grains with an opacity that depends on wavelength as λ^{-1} for long wavelenghts. Here, we describe in detail our modeling results for the NIR and MIR morphology, and SED of AB Aur.

5.1. The Thermal NIR Disk

We follow the procedure outlined in §4.1.1 to model the SED and visibilities of AB Aur. We first attempt at fitting a standard curved dust rim model (Fig 14) to the NIR visibilities. The rim is assumed to be composed of 1.3μm silicate grains and the dust evaporation temperature law is described by equation (3). This produces rim radii too large to fit baselines shorter than 100m and we had to increase the T$_{evp}$ normalization to 2800K from 2000K. This increases the sublimation temperature at the base of the rim from ∼1350K to ∼1950K. The dashed line in Fig 15 traces the visibility for this model and provides a good fit to the data at baselines shorter than 100m.

The dust-rim-only model produces large bounces in visibility beyond 150m and as in the case of MWC275, this bounce is not observed. We have scanned the 150m-300m baseline (Fig 15) range several times with CHARA and have failed to detect fringes, ruling out dust-rim only models for the AB Aur NIR emission. The addition of a Uniform Disk of emission interior to the dust destruction radius (Fig 14c) helps fit the data well (solid line in Fig 15). The gas component also helps fit the NIR SED (Fig 16). Parameters for the 'dust rim + Uniform Disk' model are listed in Table 9.

5.2. MIR SED and Emission Morphology

Liu et al. (2007) resolved the AB Aur disk at 10.3μm using nulling interferometry and measured a disk is inclination of 45°- 65° inconsistent with nearly face on measurements in the mm (Corder et al. 2005) and the NIR (Millan-Gabet et al. 2001; Eisner et al. 2004). Liu et al. (2007) interpreted their result in terms of the AB Aur circumstellar environment being more complicated than a disk. Since AB Aur is well resolved by the Keck Segment Tilting Experiment (Fig 17), a disk inclination of 45°- 65° would have produced observable size difference between the major and minor axis of the disk. We do not find evidence for this size variation in our Segment Tilting data, and hence support a face on model for the mid-infrared disk around AB Aur consistent with the NIR and mm results.

The MIR spectrum of AB Aur in the 10.7μm to 20μm range can be modeled well with a dust grain mixture of 1.3μm and 0.1μm silicates with equal mass fractions (van Boekel et al. 2005). In addition to the micron and sub-micron silicates, we include a 50μm silicate component to model the relatively flat spectrum of AB Aur between 35μm and 80μm .

Fig 18 shows a TORUS model SED that fits the MIR and longer wavelength spectrum of AB Aur well . In this model, ∼40% of the 8μm emission arises from the dust rim, with the rim contribution declining to ∼10% at 13μm. This model also fits the Keck Segment

Tilting data visibilities reproducing the 10.5±0.7AU 10μm FWHM size of AB Aur (Fig 17). By initial design, the model fits AB Aur mm-interferometry and SED.

Table 9 lists disk parameters for the AB Aur model and Fig 12 shows the radial distribution of the small grain fractions. The mid-plane temperature profile and the τ=1 surface at 5500Å are shown in Fig 13. The inner rim shadows the disk between 0.3AU and 1AU, beyond which the disk surface takes a flared geometry.

6.   Discussion

The simultaneous modeling of the infrared and millimeter SED and interferometry of MWC275 and AB Aur allows us to address several important issues regarding the structure of their circumstellar disks. To maintain clarity in our discussion we divide the disk into two regions (i) thermal NIR region (< 0.3 AU) (ii) outer disk (between 0.3AU and the disk outer edge).

6.1.   The Thermal NIR Disk

Detailed modeling (§4.1.1 and §5.1) of the inner disk shows that models where bulk of the NIR emission arises in a dust rim truncated by sublimation fail to fit the long-baseline interferometry data and under-estimate the NIR emission by a factor of 2 relative to observations. As mentioned in T08 and demonstrated in detail in this work, the presence of a gas emission component inside the dust destruction radius can solve the interferometry and SED problem simultaneously.

This however opens up a number of new questions, namely (i) What is the geometry of the gas dust transition region? To date there has been no calculation of transition region structure that treats both gas and dust simultaneously in a self consistent manner. (ii) What are the relative contributions of accretion and stellar radiation to heating the gas? We have shown that an ad-hoc addition of an NIR emission component inside the dust destruction radius helps explain the data, but the current modeling does not shed any light on the energy budget question. (iii) What are the gas species that provide the NIR opacity? Is the opacity molecular in nature or is it from free-free and free-bound processes? If a significant portion of the NIR emission were indeed arising from molecular gas, then Fig 9 shows that theoretical gas opacities depend much more sensitively on wavelength between 4 and 10μm than what is observed. This suggests that some of the molecules providing the model opacities might be getting destroyed by the stellar UV radiation field.

In the course of modeling the MWC275 and AB Aur disks, we realized (§4.1.1) that the observed K-band sizes could be reproduced only if the dust sublimation temperature at the base of the dust rims were increased to ∼1850K from the experimentally measured silicate evaporation temperatures of ∼1400K (Pollack et al. 1994). A simple treatment of the gas-dust transition region by Muzerolle et al. (2004) suggests that gas is not effective in modifying rim geometry. In the absence of shielding by gas, the large dust sublimation temperatures indicate that the grains in the inner disks of young stars are significantly more refractory and/or optically transparent than has been assumed in the literature. There is also the possibility that the gas gets optically thick along the mid-plane, shielding the dust from direct stellar radiation and allowing the dust rim to exist closer to the star (Monnier et al. 2005; Isella et al. 2006). Future, high resolution NIR spectroscopic studies of MWC275 and AB Aur, combined with self consistent models of the gas density and temperature structure, will help address many of the questions raised here.

MWC275 and AB Aur require gas emission to explain the their SED interferometry. In contrast, past modeling work by Isella et al. (2006) seems to suggest that dust rims alone are probably sufficient to explain the NIR data on the young stars V1295 Aql (A2 IVe) and CQ Tau (F2 IVe). A larger sample of young stars will therefore have to be observed with milli-arcsecond interferometry to establish and understand trends between spectral type, stellar mass, accretion rates and the contribution of gas emission to NIR SED.

A new and exciting observational domain will be opened with the commissioning of the fringe tracker (Berger et al. 2006) for CHARA-MIRC (Monnier et al. 2007) in the summer of 2008. This will sufficiently improve CHARA-MIRC sensitivities to combine light from 3 or more telescopes, allowing the first milli-arcsecond non-parametric imaging of MWC275 and AB Aur in the NIR. The snapshot multiple-baseline coverage will provide us a powerful tool in understanding the infrared time variability of YSO disks.

6.2. The Outer Disk

Our models for the MWC275 and AB Aur MIR interferometry and SED suggest that the outer disks of these systems are at different evolutionary stages. MWC275 10 micron size and MIR SED can only be reproduced if the disk is depleted in micron and sub-micron sized grains beyond ∼7AU (§4.2). This meshes well with the fact that the observed $10.7\mu m$ size of MWC275 is ∼3 times smaller than AB Aur. The depletion of small grains beyond 7AU in the disk atmosphere indicates that the dust particles in MWC275 have undergone significant settling. However, the presence of the $10\mu m$ silicate feature in MWC275 implies that there is some process (like planetesimal collisions) that maintains the supply of micron

sized grains in the inner regions of the disk.

Our models predict that the inner dust rim shadows (Dullemond & Dominik 2004) the region of the disk between 0.3AU and 1AU. The structure and size of the shadow depends sensitively on the composition of grains in the circumstellar disk (Tannirkulam et al. 2007) and hence is an important probe of dust physics. The presence of the shadow has not been observationally confirmed yet in any YSO system, although some indirect evidence has been found in VV Ser (Pontoppidan et al. 2007).

7. Conclusions

We have presented the first set of comprehensive disk models for the SED and interferometry of Herbig Ae stars MWC275 and AB Aur. We have shown that 'standard' models for the dust evaporation front where the bulk of the near-infrared emission arises from a dust wall, fail to explain the near-infrared spectral energy distribution and interferometry. Standard models produce large bounces in visibility at high spatial frequency, which is not observed in the data. We have conclusively demonstrated that the presence of an additional smooth emission component (presumably hot gas) inside the dust destruction radius and on a similar size scale to the dust rim can ameliorate the situation. In the absence of shielding of star light by gas, we have established that dust grains in the gas-dust transition region will have to be highly refractory, sublimating at 1850K. The small mid-infrared size of MWC275 relative to AB Aur, shows that the dust grains in the outer disk MWC275 are significantly more evolved/settled than the grains in the AB Aur disk. We suggest that dynamical processes (like planetesimal collisions) that maintain the population of micron-sized grains producing the 10μm feature in the spectrum, are operational only in the inner 7AU of MWC275. However, in AB-Aur the small-dust producing mechanisms exist at least out to 20 AU and maybe even beyond.

Cluster Network at the University of Michigan.

Table 1: CHARA uv coverage and visibility data for MWC275. The array geometry is illustrated in Fig 1, ten Brummelaar et al. (2005).

UT-Date of Observation	u(m)	v(m)	Telescope pair	Calibrated Visibility	Calibrator Names
2004July09	-210.61	138.79	S1W1	0.150±0.008	HD164031
	-200.38	127.78		0.143±0.009	
2005July22	106.91	-11.88	W1W2	0.218±0.011	HD164031
	103.22	-18.38		0.227±0.009	
2005July26	102.45	5.03	W1W2	0.260±0.014	HD164031
	106.45	-1.61		0.241±0.011	
	107.18	-10.26		0.201±0.011	
	105.94	-13.95		0.232±0.011	
2006June22	-11.99	84.94	S2W2	0.345±0.016	HD164031
	-24.60	85.73		0.301±0.017	
	-42.30	87.77		0.203±0.013	
2006June23	-301.23	-85.20	E1W1	0.0715±0.0043	HD164031
	-302.93	-78.34		0.0730±0.0044	
2006June23	-84.05	98.77	S2W2	0.0925±0.0041	HD164031
2006Aug23	60.15	125.48	E2S2	0.181±0.010	HD164031, HD166295
	28.16	121.90		0.189±0.011	
2007June17	-94.21	66.98	S2W1	0.232±0.013	HD164031, HD156365
	-166.86	90.88		0.080±0.005	
	-184.56	102.73		0.096±0.006	
	-195.84	114.04		0.110±0.007	

Table 2: CHARA uv coverage and visibility data for AB Aur.

UT-Date of Observation	u(m)	v(m)	Telescope pair	Calibrated Visibility	Calibrator Names
2006Aug23	212.04	237.05	E1S1	0.095±0.005	HD29645, HD31233
	203.79	251.87		0.120±0.006	
	197.53	259.95		0.123±0.007	
2006Dec14	-5.77	-325.14	E1S1	0.115±0.007	HD29645, HD31233
2006Dec15	-93.57	8.26	E2W2	0.188±0.011	HD29645, HD31233

Table 3: Keck Segment Tilting Experiment baseline coverage and uv averaged visibility data for MWC275 and AB Aur.

UT-Date of Observation	Baseline(m)	Calibrated Visibility	Calibrator Names
MWC275			
2004Sep01	3.03	0.969±0.049	v3879 Sgr
"	4.72	0.944±0.040	"
"	5.49	0.946±0.036	"
"	7.21	0.942±0.033	"
"	8.43	0.963±0.033	"
AB Aur			
2004Aug30, 31 & Sep01	3.03	0.870±0.039	iota Aur
"	4.72	0.823±0.027	"
"	5.49	0.807±0.033	"
"	7.21	0.753±0.047	"
"	8.43	0.708±0.039	"

Table 4.   Basic stellar properties and photometry for MWC275.

Property	Value
RA	17 56 21.29
Dec	-21 57 21.8
Spectral Type	A1e[a]
T_{eff}	9500K[a]
Luminosity	36 $L_\odot$[a]
Distance	122pc[a]
Mass	2.3$M_\odot$[a]
U	-
B	6.98±.08[b]
V	6.84±.06[b]
R	6.86±.05[b]
I	6.71±.07[b]
J	6.20±.08[b]
H	5.48±.07[b]
K	4.59±.08[b]

[a]Stellar parameters from Monnier et al. (2006), Natta et al. (2004) and references therein.

[b]Photometry obtained at MDM Observatories (longitude: -111.67^o, latitude:31.95^o) in 2006 June.

Table 5.   Basic stellar properties and photometry for AB Aur.

Property	Value
Spectral Type	A0pe[a]
T_{eff}	9772K[a]
Luminosity	47 $L_\odot$[a]
Distance	144pc[a]
Mass	2.4$M_\odot$[a]
U	7.18±.08[b]
B	7.14±.04[b]
V	7.01±.04[b]
R	6.96±.05[b]
I	6.70±.09 [b]
J	5.99±.05[b]
H	5.28±.05[b]
K	4.37±.05[b]

[a]Stellar parameters from Monnier et al. (2006), Isella et al. (2006) and references therein.

[b]Photometry obtained at MDM Observatories in 2005 December.

Table 6.   MWC275 disk properties from the literature

Dust Disk	
Mass	$0.0007 M_\odot$[a]
Dust to Gas Ratio	0.01
Surface Density Profile	r^{-1} [a,b]
Outer Radius	200 AU [b]
Inclination	$48^o \pm 2^o$ (this work, c)
Position Angle	$136^o \pm 2^o$ (this work, c)

Relative Mass Fractions of micron and sub-micron grains in the disk atmosphere[d]		
0.1 μm silicates	1.5 μm silicates	PAH
$0.19^{+0.009}_{-0.018}$	$0.8^{+0.05}_{-0.04}$	$0.01^{+0.001}_{-0.001}$

[a]Natta et al. (2004)

[b]Isella et al. (2007)

[c]Wassell et al. (2006)

[d]van Boekel et al. (2005)

Table 7.   AB Aur disk properties from the literature

Dust Disk	
Mass	$0.0001\mathrm{M}_\odot$[a]
Dust to Gas Ratio	0.01
Surface Density Profile	r^{-1}[b]
Outer Radius	300 AU[a]
Inclination	$21^o \pm 0.5^o$[b]
Position Angle	$58.6^o \pm 0.5^o$[b]

Relative Mass Fractions of micron and sub-micron grains in the disk atmosphere[c]		
0.1 μm silicates	1.5 μm silicates	PAH
$0.5^{+0.03}_{-0.03}$	$0.48^{+0.03}_{-0.04}$	$0.02^{+0.001}_{-0.002}$

[a]Lin et al. (2006)

[b]Corder et al. (2005)

[c]van Boekel et al. (2005)

Table 8.   MWC275 model-disk properties constrained by this work.

Dust Disk	
Inner Radius	0.22 AU[a]
K-band flux contribution from dust rim	29% [a]
Mass fractions of dust components	see Fig 12
NIR Gas Disk	
Surface Brightness Profile	constant
	(poorly constrained)
Outer Radius	0.22 AU [a]
K-band flux contribution	56% [a]
Temperature	> 1800K
Vertical Optical Depth	0.15 [a]
Gas-Opacity Profile	see Fig 9

[a]Tannirkulam et al. (2008). The star contributes 10% of the K-band flux and an extended envelope (Monnier et al. 2006) contributes 5%.

Table 9.   AB Aur model-disk properties constrained by this work.

Dust Disk	
Inner Radius	0.24 AU [a]
K-band flux contribution from dust rim	22% [a]
Mass fractions of dust components	refer Fig 12
NIR Gas Disk	
Surface Brightness Profile	constant (poorly constrained)
Outer Radius	0.24 AU [a]
K-band flux contribution	65%
Temperature	$> 1900K$
Vertical Optical Depth	0.14 [a]
Gas-Opacity Profile	refer Fig 9

[a]Tannirkulam et al. (2008). The star contributes 8% of the K-band flux and an extended envelope (Monnier et al. 2006) contributes 5%.
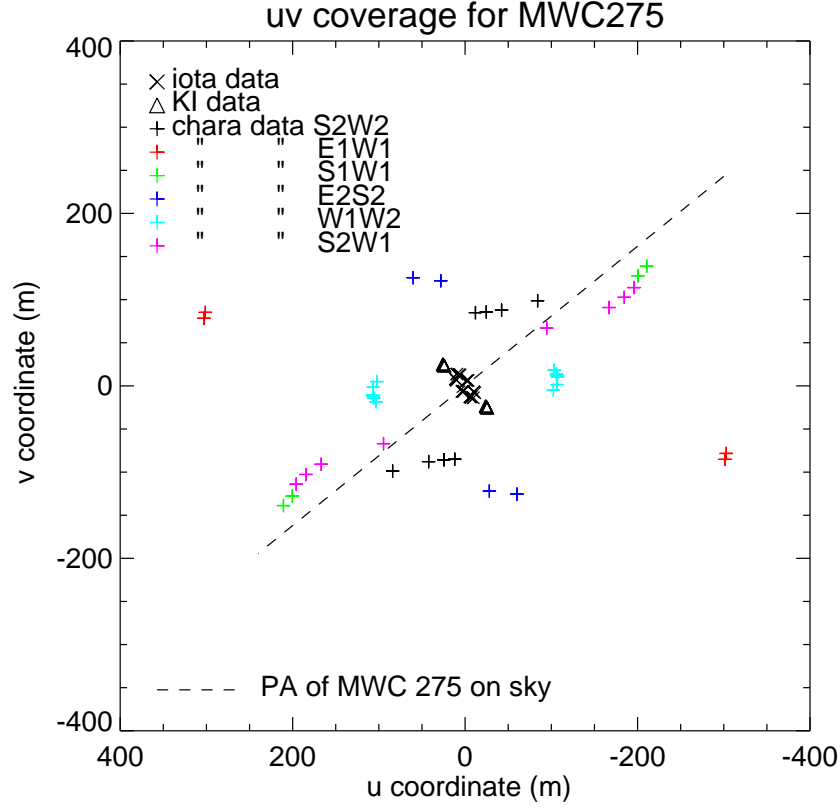
Fig. 1.— uv coverage for MWC275. We include data from KI (Monnier et al. 2005), IOTA (Monnier et al. 2006) and CHARA (Tannirkulam et al. 2008) in our analysis. A position angle (measured East of North) of 136° for MWC275 is marked in the left panel.
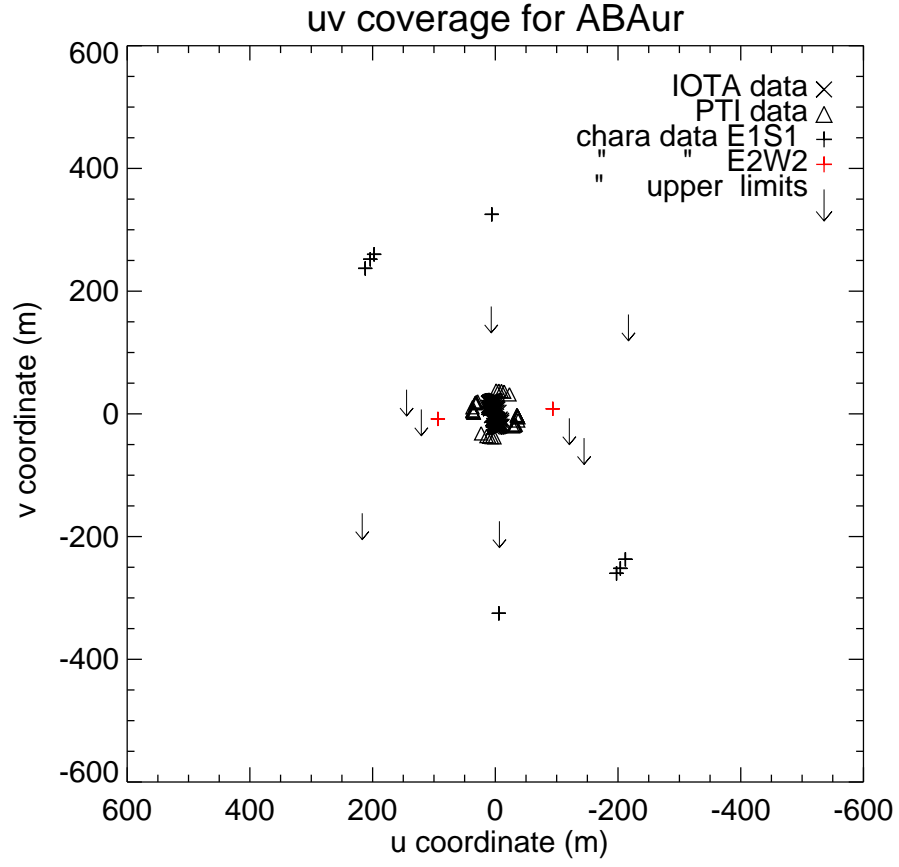
Fig. 2.— uv coverage for AB Aur. We include data from PTI (Eisner et al. 2004), IOTA and CHARA (Tannirkulam et al. 2008) in our analysis.
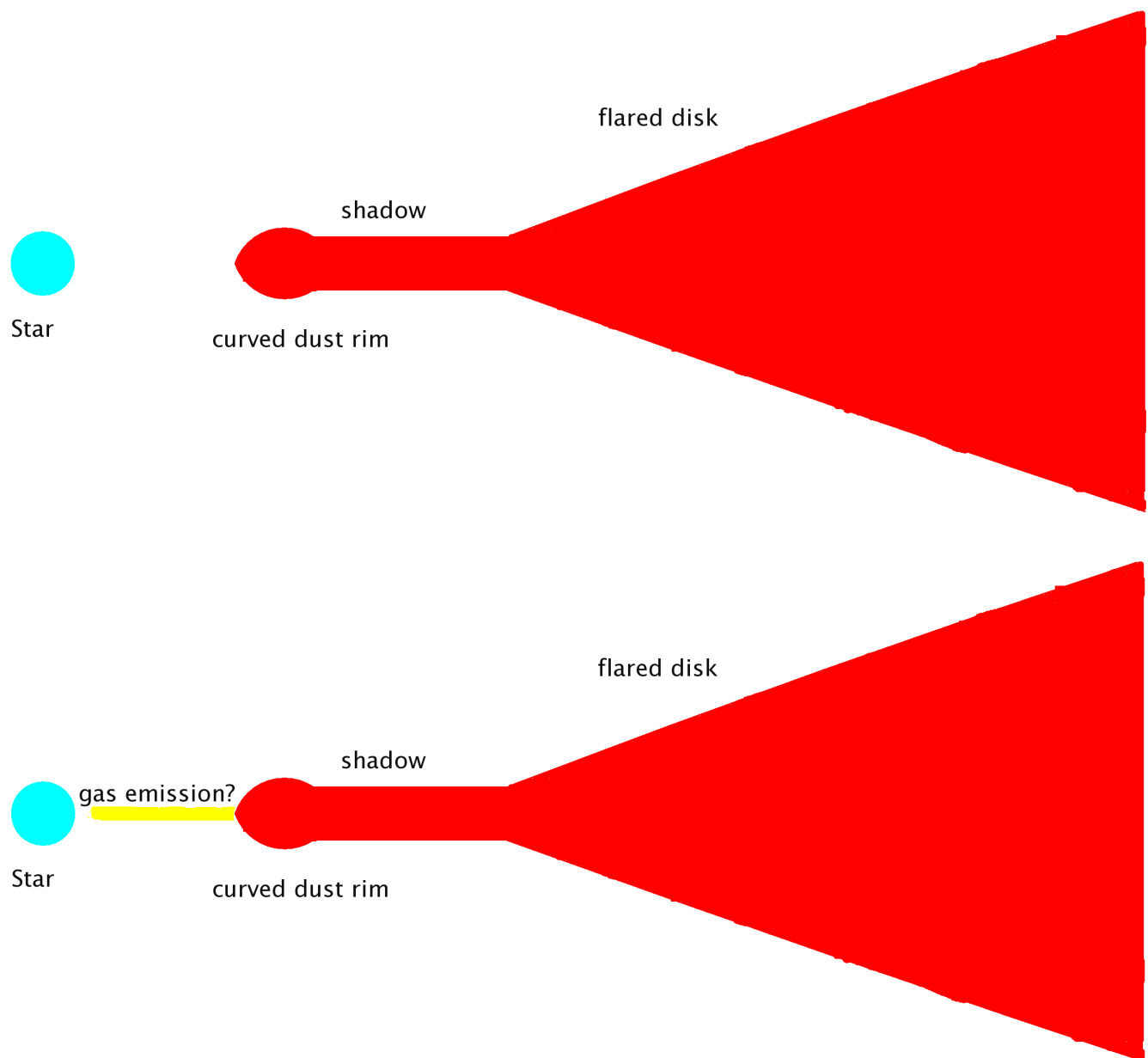
Fig. 3.— Schematic of disk models. a)Top panel. Flared disk with a curved inner rim. b) Bottom panel. An additional "smooth" emission component (presumably gas) has been added inside the dust destruction radius to explain MWC275 and AB Aur NIR photometry and interferometry.
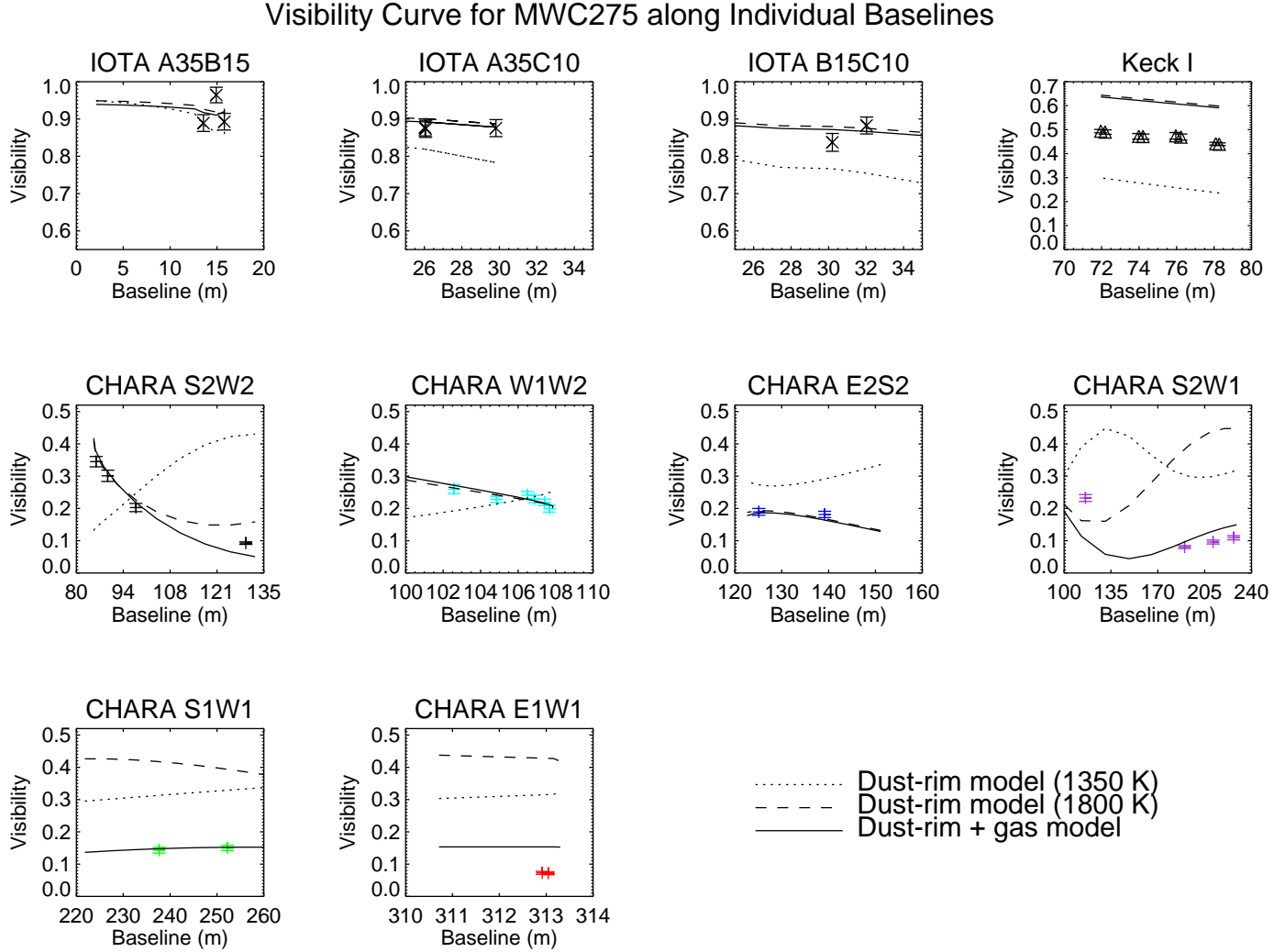
Note: The models are not to scale.

Fig. 4.— MWC 275 visibility data and model curves. The quoted model temperatures are at the base of the dust rim. The NIR size deduced from the Keck Interferometer data (triangles) is ∼20% larger than the size obtained with the CHARA data. This variability of MWC275 is discussed in §4.1.2.
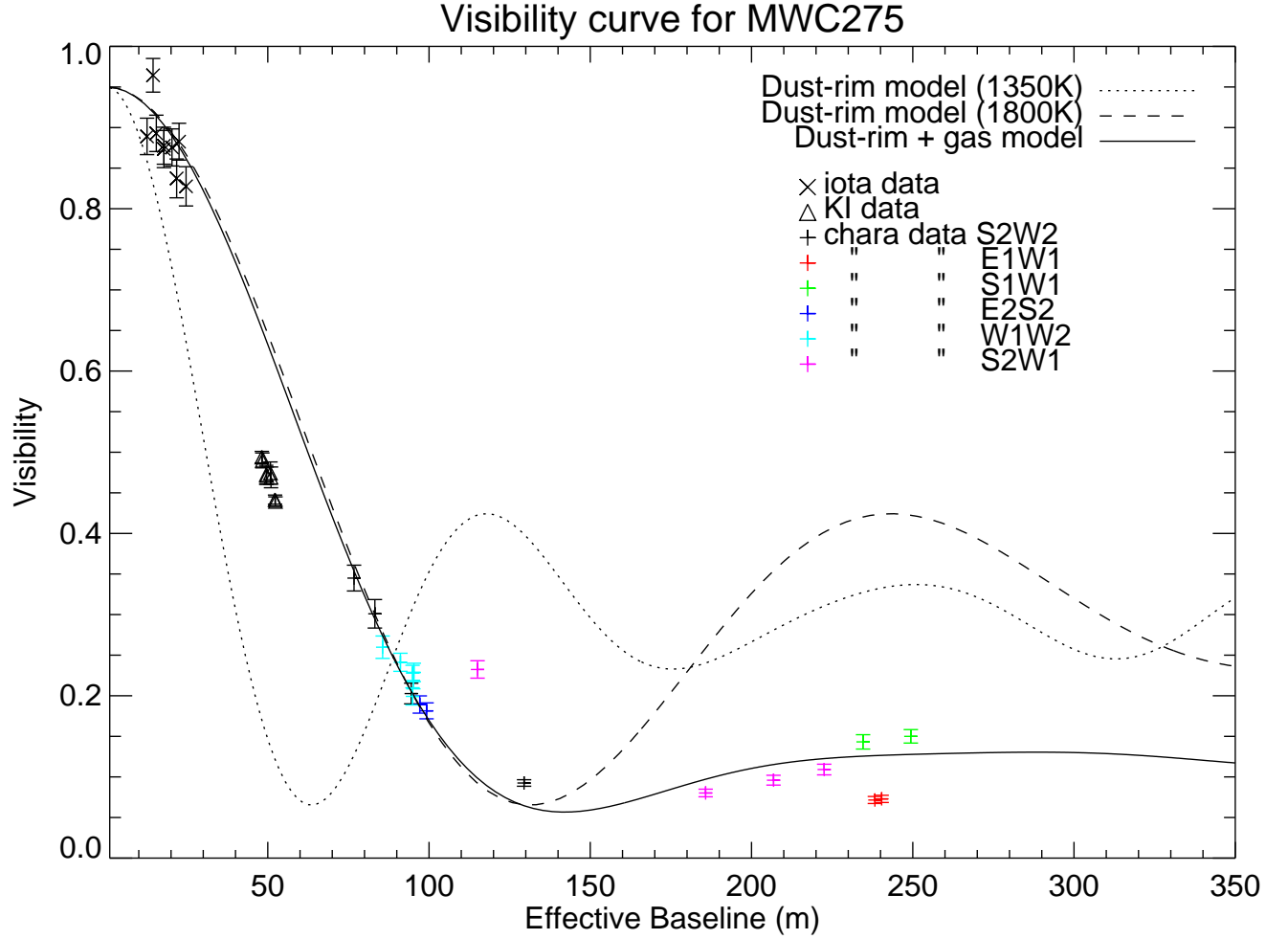
Fig. 5.— MWC275 visibility vs 'Effective Baseline'. Effective Baselines are useful in presenting data along multiple uv vectors in a concise manner (under the assumption of axial symmetry). The NIR size deduced from the Keck Interferometer data (triangles) is ∼20% larger than the size obtained with the CHARA data. This variability of MWC275 is discussed in §4.1.2
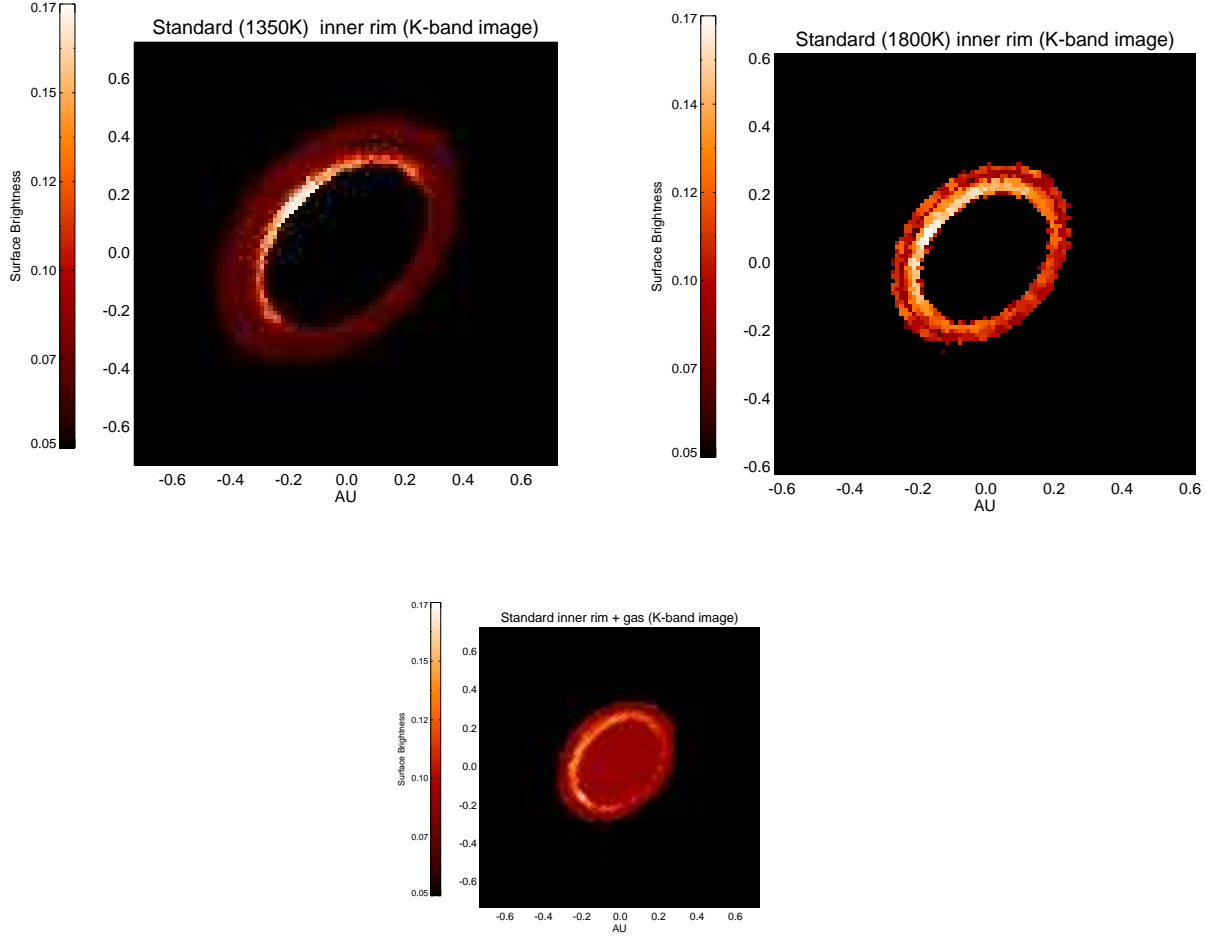
Fig. 6.— Inclined-disk models for NIR emission in MWC275. The disk has an inclination of 48° and a PA of 136° (North is towards the top and East is on the left). The sense of the inclination is from Grady et al. (1999) a) Top left panel. A standard curved dust-rim-only model with rim-base temperature ∼1350K. b) Top right panel. Standard curved dust-rim-only model with rim-base temperature ∼1800K. c) Bottom panel. Curved dust-rim model with gas emission (modeled as a uniform disk centered on the star) inside the dust rim to smooth out the emission profile.
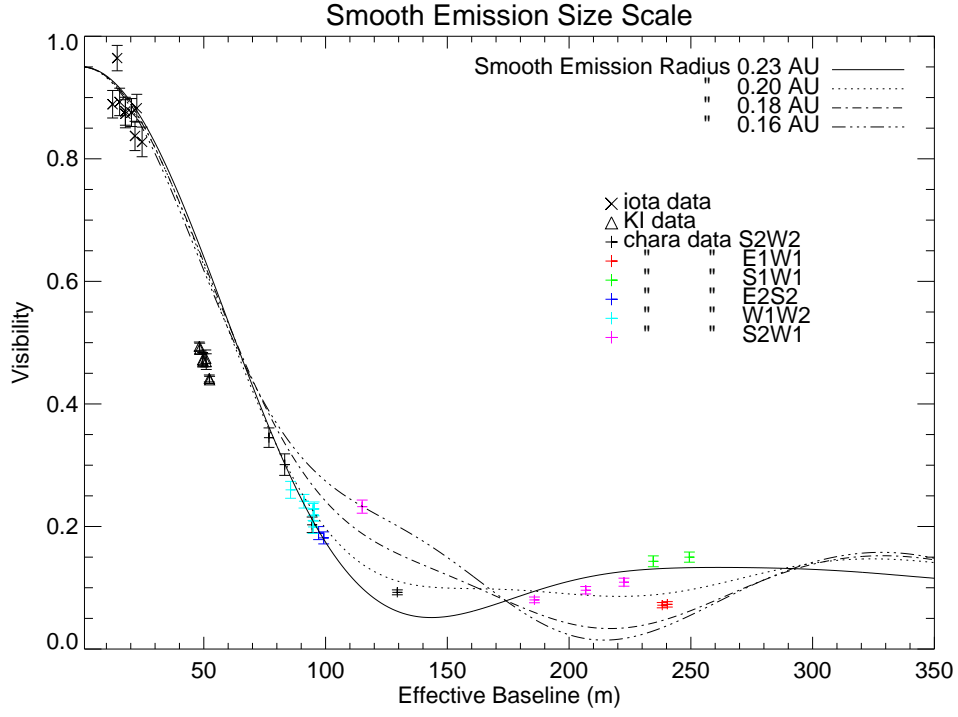
Fig. 7.— Constraining the size scale of the smooth emission component interior to the dust destruction radius in MWC275. The model visibilities begin to deviate significantly from the data when the radius of the smooth emission component becomes smaller than 0.19 AU.
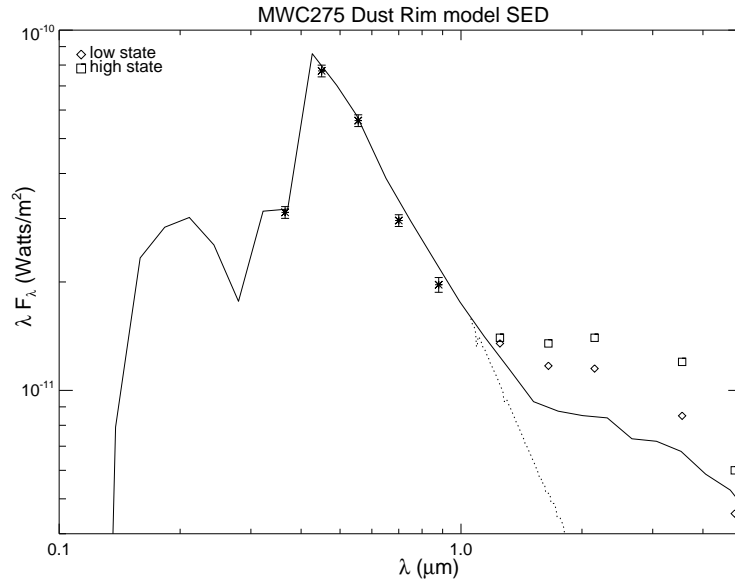
Fig. 8.— The NIR SED for MWC275. The 'stars' are photometry points from MDM (Appendix Table 4). The 'squares' and 'diamonds' are high and low state measurements from Sitko et al. (2008). The solid line is the SED produced by the 'star + dust-rim only' model in Fig 6b. The dotted line is the SED of the star.
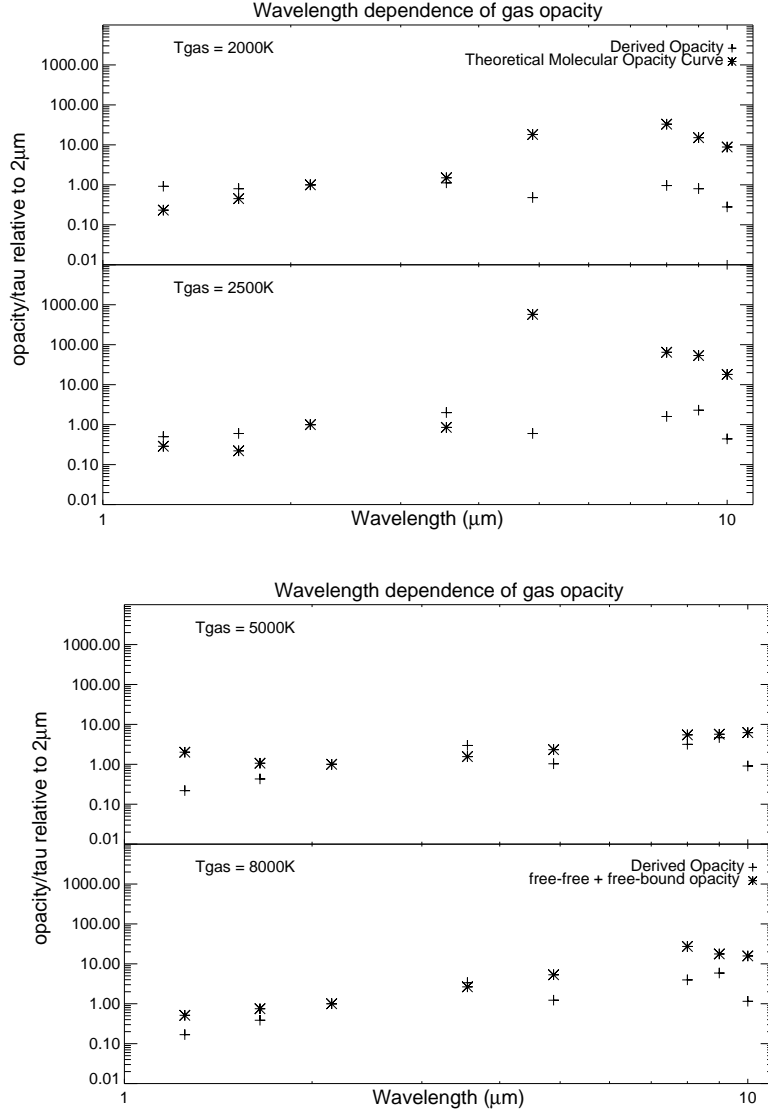
Fig. 9.— The plusses (+) represent empirically derived gas opacities from observed photometry and NIR disk models for MWC275 (see Fig 6). a) Top panel. The stars represent fiducial theoretical molecular absorption opacities smoothed over the photometry band for 2000K and 2500K gas respectively (Zhu et al. 2007). The opacity jump at 5μm is due to water vapor. b) Bottom Panel. The gas absorption opacity at infrared wavelengths is dominated by free-free and free-bound transitions of H^- at 5000K and by hydrogen at 8000K (Ferguson et al. 2005; Zhu et al. 2007).

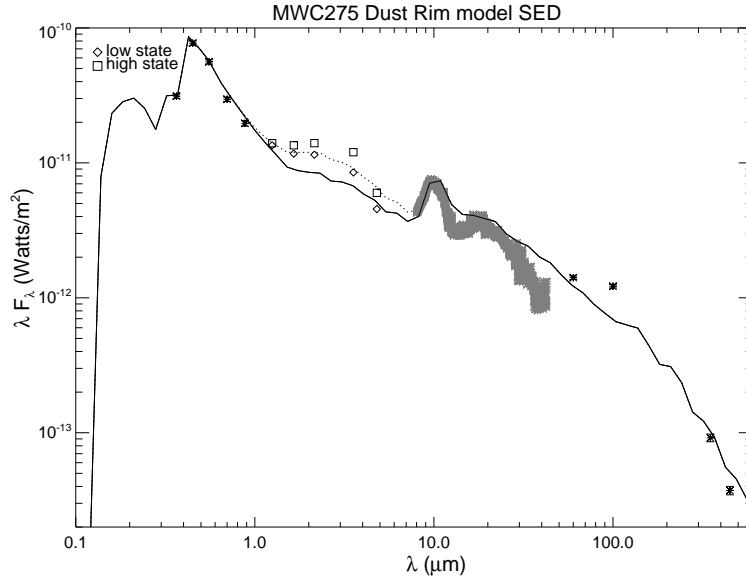Fig. 10.— MWC275 SED from UV to mm.The mid, far-infrared and sub-mm data are from Meeus et al. (2001) and references therein. The solid line traces the dust-disk model SED (see §4.2). The dotted line traces the dust-disk+smooth emission SED. The smooth component is modeled as optically-thin grey emission at 2500K. The relative contributions of star, dust and gas to the total integrated flux are 0.79, 0.16 and 0.05 respectively.
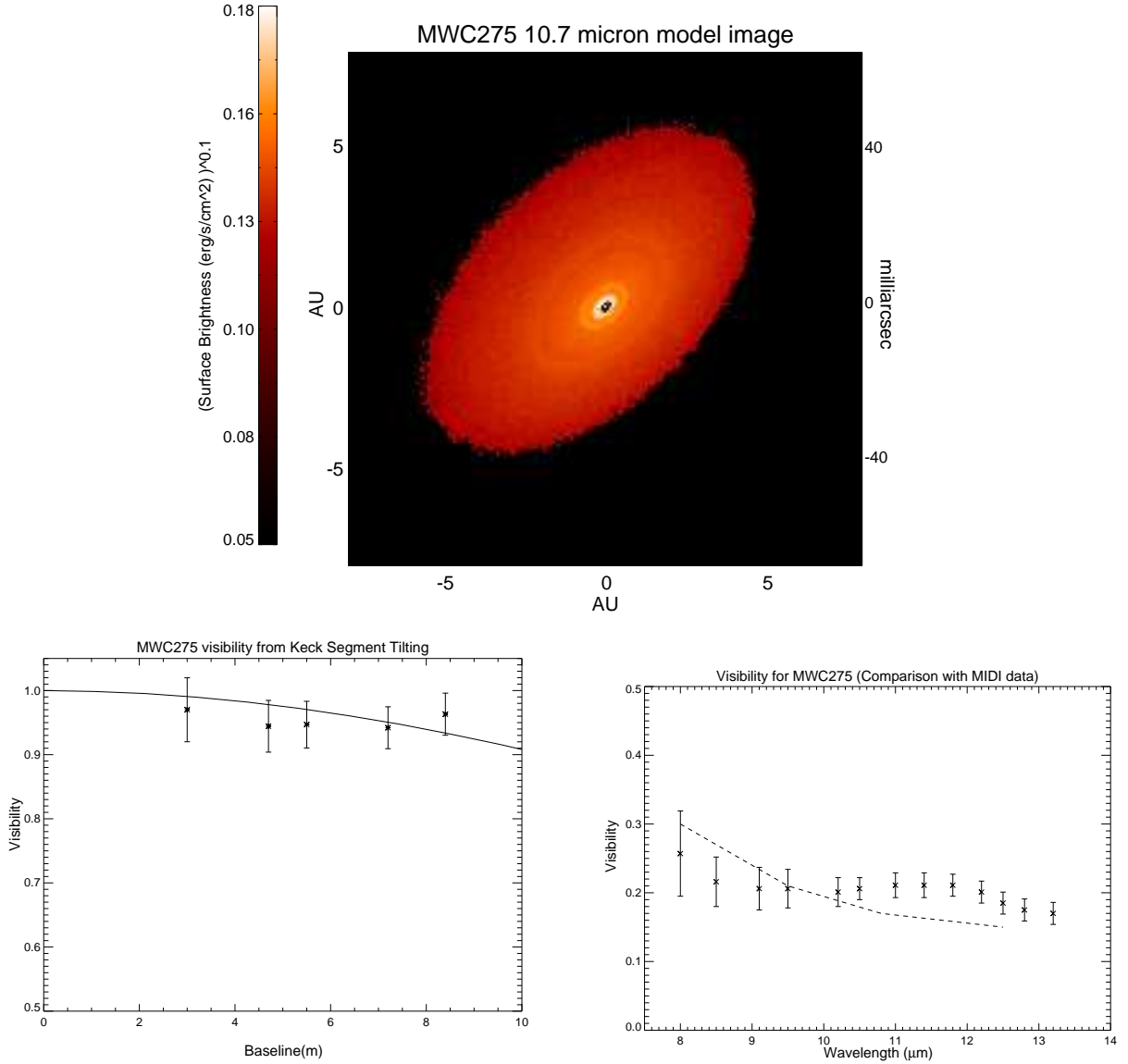
Fig. 11.— MIR image and visibilities for MWC275. The disk has an inclination of 48° and a PA of 136° (North is towards the top and East is on the left) a) Top panel. Synthetic 11μm TORUS image. b) Bottom left panel. Azimuthally averaged 10.7μm visibilities from the Keck Segment Tilting Experiment (Monnier et al. 2008). The 'stars' are measured values and the solid line is the model visibility. MWC275 is not resolved by Keck. c) Bottom right panel. Model visibilities compared with MIDI (Leinert et al. 2004) data. The MIDI data was obtained at a projected baseline of ~ 99m and a PA of 16°, nearly aligned with disk minor axis.
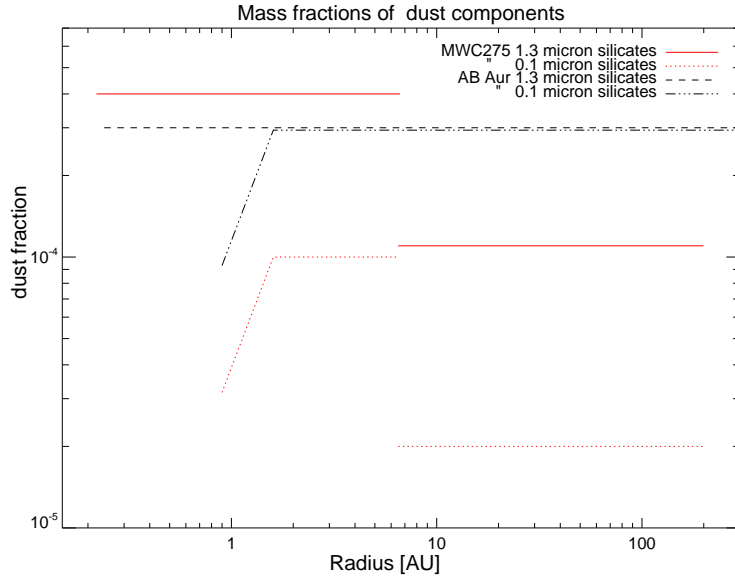
Fig. 12.— Mass fractions of dust components relative to gas. The micron and sub-micron grain fraction in MWC275 (red solid and dotted lines) have to be reduced below 20% of their values inside of 6.5AU at larger radii to fit the SED and interferometry. The silicate-grain opacities are from Ossenkopf et al. (1992) and the relative masses of dust grains are from van Boekel et al. (2005). Between 0.9AU and 1.6 AU, 0.1μm grains are added smoothly to avoid the formation of two distinct dust rims.

Bulk of the dust mass is in mm sized grains with a power law opacity profile (Natta et al. 2004). For AB Aur, we also add a 50μm silicate component to improve SED fits between 40μm and $100mu$m. The dust parameters are derived assuming gas and dust are well mixed.
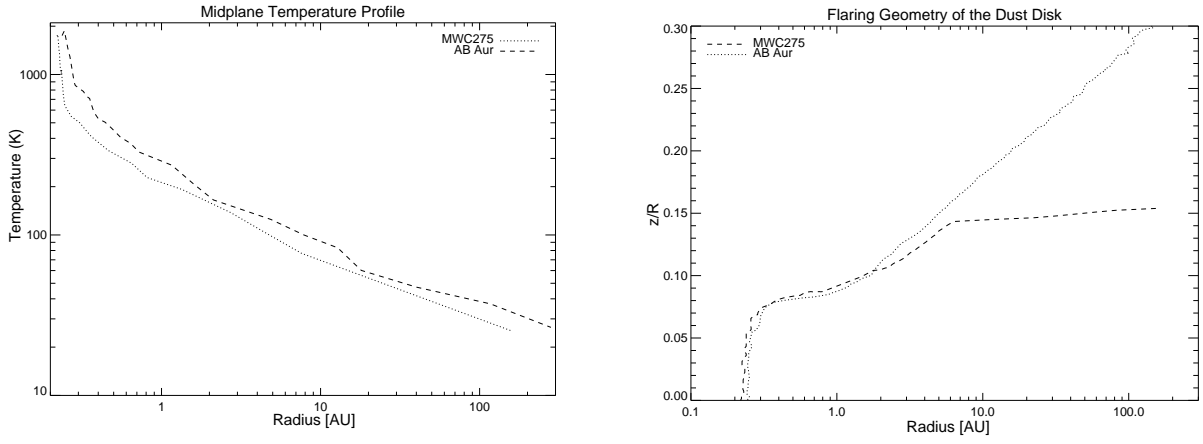
Fig. 13.— Temperature profile and disk-surface shapes for MWC275 and AB Aur. a) Left panel. Midplane temperature profile for MWC275 (dotted line) and AB Aur (dashed line). b) Right panel. The figure shows τ=1 at 5500Å surface of the disk measured along radial lines from the central star. The y axis is the polar angle (0 is the equatorial plane) in radians.
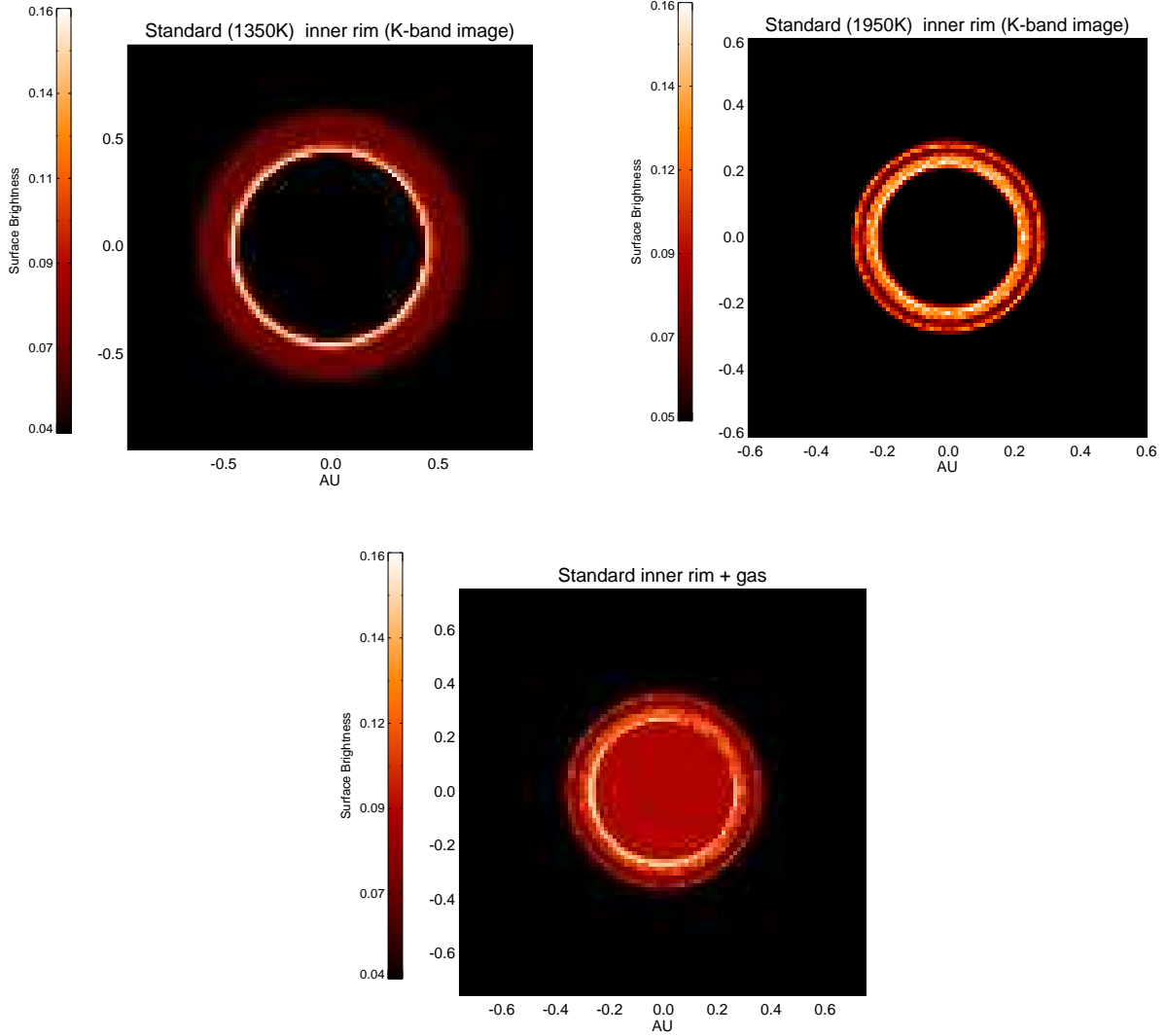
Fig. 14.— Face-on models for NIR emission in AB Aur. a) A standard curved dust-rim-only model with rim-base temperature ∼1350K. b) Top right panel. Standard curved dust-rim-only model with rim-base temperature ∼ 1950K. c) Bottom panel. Curved dust-rim model with gas emission (modeled as a uniform disk centered on the star) added inside the dust rim in to smooth out the emission profile. The central star has been suppressed in all the panels.
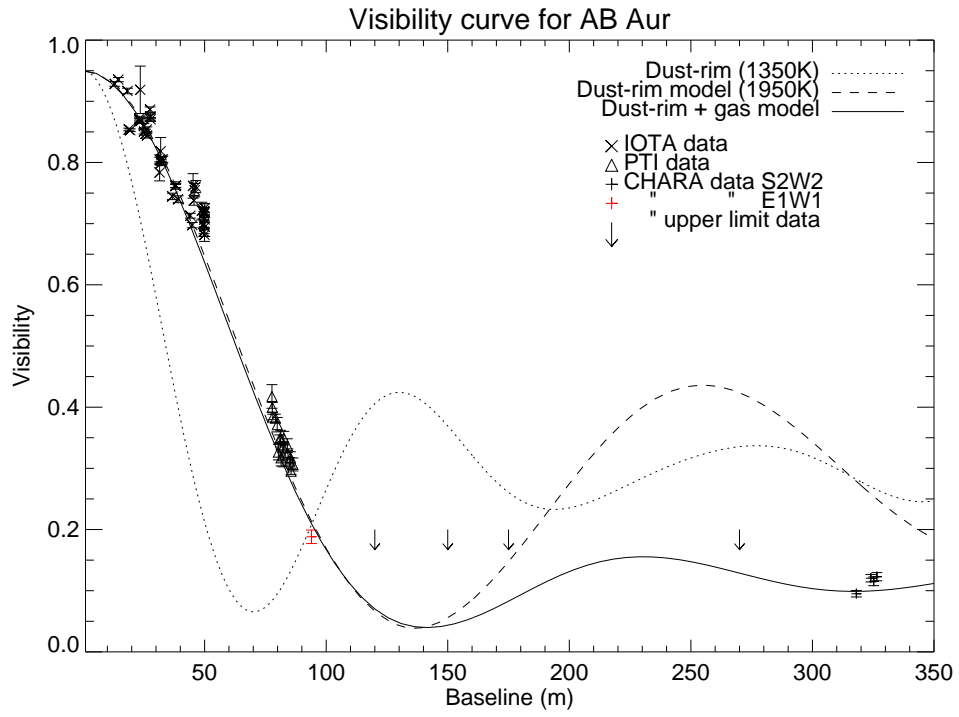
Fig. 15.— AB Aur visibility vs Baseline. The arrows are upper limits on the visibility. The quoted model temperatures are at the base of the dust rims.
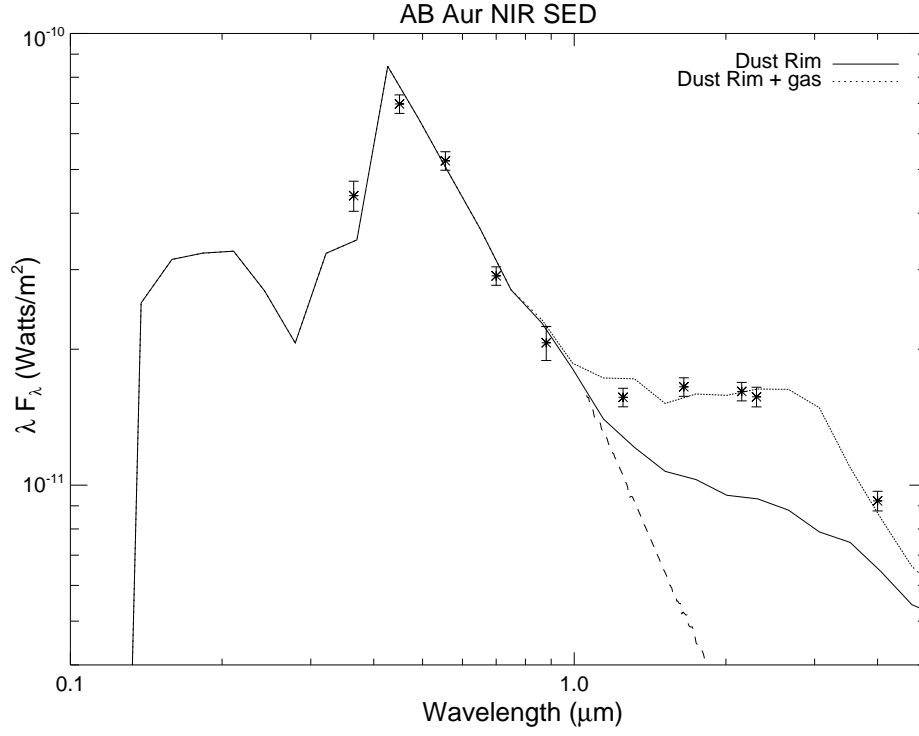
Fig. 16.— The NIR SED for AB Aur. The 'stars' are photometry points from MDM (Table 5). The solid line is the SED produced by the 'star + dust-rim only' model in Fig 14b. The dashed line traces the stellar SED. The dotted line includes emission from gas at 2500K, assuming that the gas opacity curve derived for MWC275 (see Fig. 9) is valid for AB Aur as well.
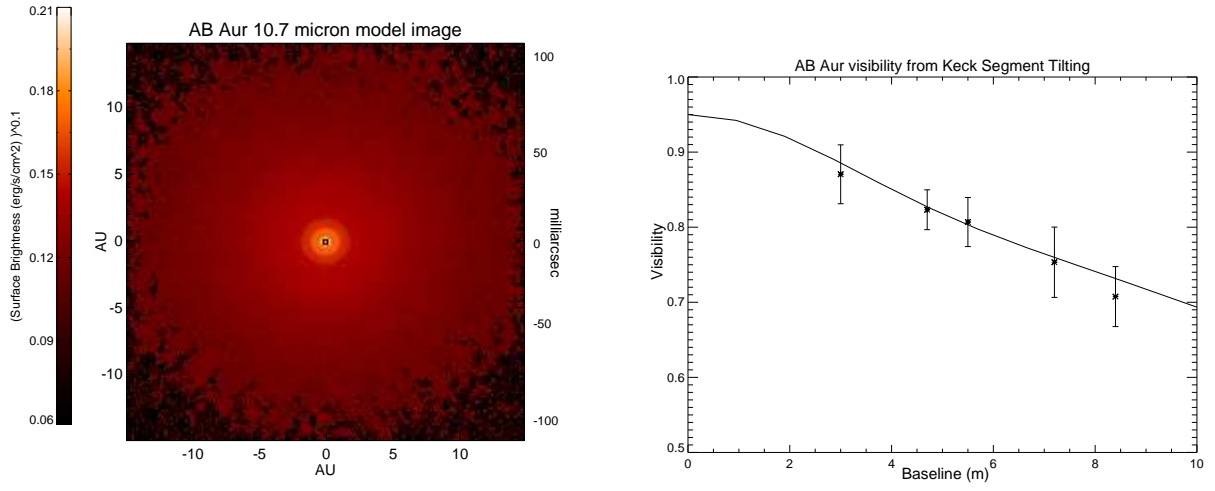
Fig. 17.— 10.7μm image and visibilities for AB Aur. a) Left panel. Synthetic 10.7μm TORUS image b)Right panel. Model visibilities (solid line) compared with azimuthally averaged Keck Segment Tilting data (Monnier et al. 2004). The model also includes 5% emission arising from an extended envelope.
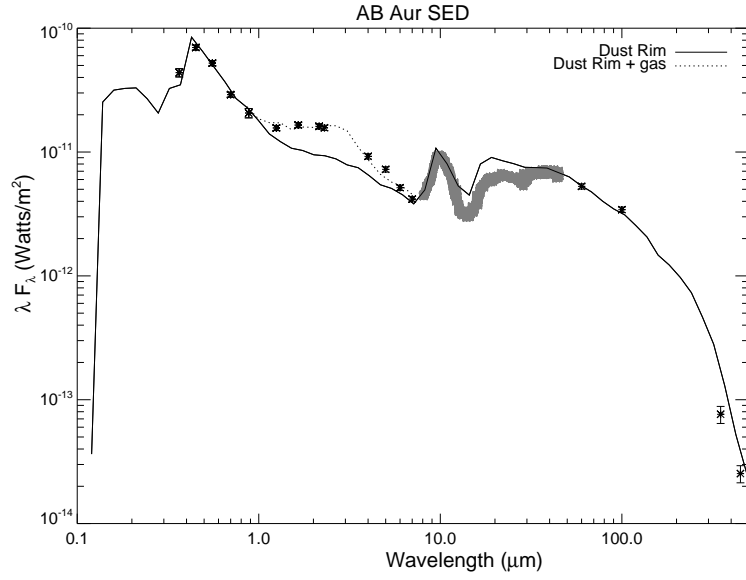
Fig. 18.— AB Aur SED from UV to mm. The mid, far-infrared and sub-millimeter data are from Meeus et al. (2001) and references therein. The solid line traces the dust-disk model SED (see §5.2). The dotted line traces the dust-disk + gas model. The relative contributions of star, dust and gas to the total integrated flux are 0.67, 0.27 and 0.06 respectively.

A. Appendix

A.1. Photometry

Table 10:: UBVRI Photometry. Majority of the MDM targets are YSOs.

| Target	RA (J2000)	Dec	U	B	V	R	I	UT Date of Observation
HIP 2080	00 26 16.5	+ 03 49 33	-	6.72±0.05	6.81±0.04	6.94±0.06	6.93±0.04	08/27/2006
HIP2370	00 30 16.4	− 29 14 38	-	12.65±0.05	12.28±0.04	12.13± 0.06	11.75±0.04	"
HIP3013	00 38 20.3	−14 59 54	-	10.67±0.05	10.86± 0.04	6.95± 0.06	11.07±0.04	"
BP Tau	04 19 15.8	+ 29 06 27	13.20± 0.15	13.36±0.03	12.32±0.04	11.45±0.04	10.60±0.04	11/29/2004
CI Cam	04 19 42.1	+55 59 57	12.13±0.07	12.41 ±0.06	11.77±0.05	10.79± 0.05	9.99±0.04	11/27/2004
			12.32±0.08	12.70 ±0.04	11.75±0.05	10.64±0.05	9.82±0.09	12/10/2005
			-	12.59±0.05	11.71± 0.03	10.72± 0.04	9.94±0.05	08/28/2006
DG Tau	04 27 04.7	+26 06 16	13.93±0.04	13.97±0.03	12.79± 0.04	11.70± 0.04	10.67±0.04	11/29/2004
DI Tau	04 29 42.5	+26 32 49	16.06±0.25	14.45± 0.03	12.96 ± 0.04	11.87± 0.04	10.70±0.04	"
V830 Tau	04 33 10.0	+24 33 43	14.66±0.15	13.52± 0.03	12.21 ± 0.04	11.26± 0.04	10.44±0.04	"
LkCa 15	04 39 17.8	+22 21 03	13.98±0.07	13.30± 0.03	12.09 ± 0.04	11.26± 0.04	10.52±0.04	"
GM Aur	04 55 11.0	+30 21 59	13.90±0.04	13.38±0.03	12.19 ± 0.04	11.34± 0.04	10.61±0.04	"
AB Aur	04 55 45.8	+30 33 04	7.18 ±0.08	7.14 ±0.04	7.01 ± 0.04	6.96 ± 0.05	6.70±0.09	12/10/2005
			-	7.19 ±0.05	7.05± 0.05	7.01± 0.06	6.80±0.04	08/27/2006
MWC480	04 58 46.3	+29 50 37	-	7.91 ±0.05	7.68± 0.03	7.62± 0.05	7.45±0.05	08/28/2006
UX Ori	05 04 30.0	−03 47 14	10.93 ±0.07	10.70±0.06	10.33±0.05	10.07± 0.05	9.75±0.04	11/29/2004
			10.43± 0.08	10.22±0.04	9.97± 0.04	9.87± 0.05	9.56±0.09	12/10/2005
RW Aur	05 07 49.5	+30 24 05	10.86±0.04	11.07± 0.03	10.32± 0.04	9.78± 0.04	9.17±0.04	11/29/2004
GW Ori	05 29 08.4	+11 52 13	11.60± 0.04	11.29±0.03	10.16± 0.04	9.38± 0.04	8.75±0.04	11/29/2004
MWC 758	05 30 27.5	+25 19 57	8.59 ± 0.07	8.56 ±0.06	8.28± 0.05	8.11± 0.05	7.95±0.04	11/29/2004
			-	8.58 ± 0.05	8.28± 0.03	8.15± 0.04	7.92±0.05	08/28/2006
V380 Ori*	05 36 25.4	−06 42 58	10.29±0.07	10.43±0.06	10.06±0.05	9.67± 0.05	8.99±0.04	11/29/2004
			10.07± 0.08	10.15±0.04	9.74± 0.04	9.38 ± 0.05	8.80±0.09	08/27/2008
FU Ori	05 45 22.4	+09 04 12	-	10.80±0.08	9.52± 0.15	8.63± 0.05	8.11±0.15	11/29/2004
			11.57±0.08	10.81±0.04	9.47± 0.04	8.60± 0.05	7.89±0.09	12/10/2005
			-	10.87±0.05	9.65± 0.03	8.87± 0.05	8.13±0.05	08/28/2006
HD 45677	06 28 17.4	−13 03 11	7.03±0.07	7.56±0.06	7.51± 0.05	7.33± 0.05	7.24±0.04	11/27/2004
			6.99±0.08	-	7.52± 0.04	7.35± 0.05	7.06±0.09	12/10/2005
MWC 147	06 33 05.2	+10 19 20	8.45±0.07	8.87±0.06	8.65± 0.05	8.30± 0.05	8.02±0.04	11/27/2004
Z CMa	07 03 43.2	-11 33 06	9.78±0.07	9.86±0.06	9.17± 0.05	8.50± 0.05	7.75±0.04	"

Table 10:: UBVRI Photometry. Majority of the MDM targets are YSOs.

Target	RA (J2000)	Dec	U	B	V	R	I	UT Date of Observation
MWC 166	07 04 25.5	-10 27 16	7.08±0.07	7.55±0.06	7.16± 0.05	6.97± 0.05	6.65±0.04	"
HD 58647	07 25 56.1	−14 10 44	6.66±0.07	6.874±0.06	6.73± 0.05	6.76± 0.05	6.67±0.04	"
IRC+10216	09 47 59.4	+13 16 44	-	-	>15.9	15.60±0.10	12.52±0.04	"
Beta Leo	11 49 03.6	+14 34 19	-	2.36±0.09	2.18±0.08	2.17±0.09	2.22±0.07	06/09/2006
HD141569	15 49 57.8	−03 55 16	-	7.32±0.09	7.16±0.08	7.14 ±0.09	7.15±0.07	"
			-	7.32±0.05	7.14±0.04	7.23± 0.06	7.03±0.04	08/27/2006
HD142666	15 56 40.0	−22 01 40	-	9.70±0.05	9.05±0.04	8.77±0.06	8.32±0.04	08/28/2006
HD143006	15 58 36.9	−22 57 15	-	10.94±0.09	10.12±0.08	9.63±0.09	9.38±0.07	06/09/2006
			-	10.95± 0.05	10.14±0.04	9.75 ±0.06	9.22±0.04	08/28/2006
HD144432	16 06 58.0	−27 43 10	-	8.57 ±0.09	8.21 ±0.08	7.98±0.09	7.96±0.07	06/09/2006
			-	8.62 ±0.05	8.20 ±0.03	7.97±0.04	7.83±0.04	08/28/2006
HD150193 (MWC863)	16 40 17.9	−23 53 45	-	9.43 ±0.09	8.87±0.08	8.48±0.09	8.20±0.07	06/09/2006
			-	9.42 ±0.05	8.87±0.04	8.58±0.06	8.04±0.04	08/27/2006
KKOph	17 10 08.0	−27 15 18	-	12.77±0.09	12.11±0.08	11.61±0.09	11.16±0.07	06/09/2006
HD158352	17 28 49.7	+00 19 50	-	5.67 ±0.05	5.38 ±0.04	5.33±0.06	5.18±0.04	08/27/2006
HD158643	17 31 25.0	−23 57 45	-	4.81 ± 0.09	4.78 ±0.08	4.80±0.09	4.73±0.07	06/09/2006
			-	4.87 ±0.05	4.78 ±0.03	4.81 ±0.04	4.62±0.04	08/28/2006
RSOph	17 50 13.2	−06 42 28	-	12.65 ± 0.08	11.43 ±0.06	10.21±0.05	9.51±0.07	06/08/2006
MWC275	17 56 21.3	−21 57 22	-	6.98 ±0.08	6.84 ±0.06	6.86 ±0.05	6.71±0.07	"
			-	7.01 ±0.05	6.86 ±0.04	6.90 ±0.06	6.72±0.04	08/27/2006
HD169412	18 21 33.5	+52 54 08	-	7.89 ±0.09	7.82 ±0.08	7.85±0.09	7.97±0.07	06/09/2006
MWC297	18 27 39.6	−03 49 52	-	14.38 ±0.09	12.26 ± 0.08	10.29±0.09	9.10±0.07	"
			-	14.27 ± 0.05	12.23 ± 0.04	10.30±0.06	8.92±0.04	08/27/2006
VVSer	18 28 47.9	+00 08 40	-	13.23 ±0.08	12.22 ±0.06	11.36±0.05	10.61±0.07	06/08/2006
MWC 300	18 29 25.7	−06 04 37	-	12.87±0.09	11.82 ±0.08	11.01±0.09	10.56±0.07	06/09/2006
RCra	19 01 53.7	−36 57 08	-	12.17±0.05	11.45 ±0.03	10.82±0.05	10.15±0.05	08/28/2006
TCra	19 01 58.8	−36 57 50	-	13.67±0.05	12.50 ±0.03	11.87±0.05	11.23±0.05	"
MWC614	19 11 11.3	+15 47 16	-	7.50 ±0.05	7.37 ±0.04	7.41±0.06	7.26±0.04	08/27/2006
HIP96720	19 39 41.4	+14 02 53	-	11.06±0.05	10.65 ± 0.03	10.38±0.05	10.06±0.05	08/28/2006

Table 10:: UBVRI Photometry. Majority of the MDM targets are YSOs.

Target	RA (J2000)	Dec	U	B	V	R	I	UT Date of Observation
V1295 Aql	20 03 02.5	+05 44 17	-	7.85 ±0.08	7.79 ±0.06	7.69±0.05	7.59±0.07	06/08/2006
			-	7.93±0.05	7.80 ±0.04	7.77±0.06	7.58±0.04	08/27/2006
V1685Cyg	20 20 28.2	+41 21 52	-	11.63±0.09	10.79 ± 0.08	10.06±0.09	9.58±0.07	06/09/2006
MWC342	20 23 03.6	+39 29 50	-	11.88±0.09	10.57±0.08	9.44±0.09	8.72±0.07	”
V1057 Cyg	20 58 53.7	+44 15 28	16.00±0.28	14.32±0.06	12.50 ± 0.05	11.18± 0.05	9.78±0.04	11/27/2004
MWC361	21 01 36.9	+68 09 48	-	7.75±0.05	7.33 ±0.03	7.00±0.04	6.62±0.05	08/28/2006
AS 477	21 52 33.9	+47 13 38	10.48± 0.07	10.52± 0.06	10.07 ±0.05	9.85±0.05	9.50±0.04	11/27/2004
HIP113937	23 04 23.6	−24 06 56	-	9.12±0.05	9.07 ±0.04	9.18±0.06	9.08±0.04	08/27/2006
HIP114547	23 12 09.4	−25 24 14	-	9.51±0.05	9.12 ±0.04	8.98± 0.06	8.67±0.04	”
HIP115858	23 28 25.2	−25 25 14	-	7.09±0.05	6.88 ±0.04	6.92± 0.06	6.72±0.04	”

Table 11:: JHK Photometry. Majority of the MDM targets are YSOs.

Target	RA (J2000)	Dec	J	H	K	UT Date of Observation
V892Tau	04 18 40.6	+28 19 16	8.61±0.05	7.08±0.05	5.86±0.05	12/17/2005
BP Tau	04 19 15.8	+29 06 27	9.10±0.10	8.37±0.10	7.90±0.10	12/01/2004
			9.05±0.05	8.32±0.05	7.85±0.05	12/17/2005
CI Cam	04 19 42.1	+55 59 58	7.20±0.10	5.68±0.10	4.44±0.10	12/01/2004
			7.01±0.05	5.63±0.05	4.35±0.05	12/17/2005
DG Tau	04 27 04.7	+26 06 16	8.92±0.05	7.95±0.05	7.15±0.05	12/17/2005
V830 Tau	04 33 10.0	+24 33 43	9.36±0.05	8.73±0.05	8.52±0.05	12/17/2005
LkCa 15	04 39 17.8	+22 21 04	9.33±0.05	8.72±0.05	8.23±0.05	12/17/2005
GM Aur	04 55 11.0	+30 22 00	9.40±0.05	8.80±0.05	8.52±0.05	12/17/2005
AB Aur	04 55 45.8	+30 33 04	5.99±0.05	5.28±0.05	4.37±0.05	12/17/2005
MWC480	04 58 46.3	+29 50 37.0	6.90±0.05	6.38±0.05	5.57±0.05	12/17/2005
RW Aur	05 07 49.5	+30 24 05	8.22±0.05	7.67±0.05	7.16±0.05	12/01/2004
			8.34±0.10	7.66±0.10	7.18±0.10	12/17/2005
GW Ori	05 29 08.4	+11 52 13	7.42±0.05	6.67±0.05	5.83±0.05	12/17/2005
MWC 758	05 30 27.5	+25 19 57	7.20±0.10	6.55±0.10	5.80±0.10	12/01/2004
			7.26± 0.05	6.70±0.05	5.92±0.05	12/17/2005
MWC120	05 41 02.3	−02 43 00	7.24±0.05	6.66±0.05	5.77±0.05	12/17/2005
FU Ori	05 45 22.4	+09 04 12	6.55±0.05	5.89±0.05	5.32±0.05	12/17/2005
HD 45677	06 28 17.4	−13 03 11	6.85±0.05	6.22±0.05	4.61±0.05	12/17/2005
MWC 147	06 33 05.2	+10 19 20	7.34±0.05	6.70±0.05	5.73±0.05	12/17/2005
Z CMa	07 03 43.2	−11 33 06	6.66±0.05	5.45±0.05	3.94±0.05	12/17/2005
MWC 166	07 04 25.5	−10 27 16	6.32±0.05	6.32±0.05	6.27±0.05	12/17/2005
Beta Leo	11 49 03.6	+14 34 19	1.92±0.08	1.96±0.07	1.90±0.08	06/02/2006
LambdaVir	14 19 06.6	−13 22 16	4.26±0.08	4.25±0.07	4.20±0.08	”
HD141569	15 49 57.8	−03 55 16	6.67±0.08	6.54±0.07	6.48±0.08	06/02/2006
HD143006	15 58 36.9	−22 57 15	8.18±0.08	7.57±0.07	5.94±0.08	06/02/2006
HD144432	16 06 58.0	−27 43 10	7.23±0.08	6.69±0.07	6.14±0.08	06/02/2006
HD150193 (MWC863)	16 40 17.9	−23 53 45	6.84±0.08	6.02±0.07	5.13±0.08	06/02/2006
KKOph	17 10 08.1	−27 15 18	8.46±0.08	7.09±0.07	5.71±0.08	06/02/2006

Table 11:: JHK Photometry. Majority of the MDM targets are YSOs.

Target	RA (J2000)	Dec	J	H	K	UT Date of Observation
HD158643	17 31 25.0	−23 57 46	4.76±0.08	4.63±0.07	4.34±0.08	06/02/2006
RSOph	17 50 13.2	−06 42 29	7.94±0.08	7.17±0.07	6.77±0.08	06/04/2006
MWC275	17 56 21.3	−21 57 22	6.20±0.08	5.48±0.07	4.59±0.08	06/02/2006
HD169412	18 21 33.5	+52 54 08	7.77±0.08	7.78±0.07	7.79±0.08	06/02/2006
MWC297	18 27 39.6	−03 49 52	6.06±0.08	4.54±0.07	3.12±0.08	06/04/2006
VVSer	18 28 47.9	+00 08 40	8.60±0.08	7.37±0.07	6.20±0.08	06/02/2006
MWC614	19 11 11.3	+15 47 16	6.91±0.08	6.58± 0.07	5.88±0.08	06/03/2006
V1295Aql	20 03 02.5	+05 44 17	7.15±0.08	6.61±0.07	5.75±0.08	06/02/2006
V1685Cyg	20 20 28.3	+41 21 52	7.97±0.05	7.01±0.05	5.86±0.05	12/17/2005
			7.93±0.10	6.96±0.04	5.81±0.07	06/03/2006
MWC342	20 23 03.6	+39 29 50	7.01±0.05	5.98±0.05	4.78±0.05	12/17/2005
			6.94±0.08	5.92±0.08	4.65±0.08	06/03/2006
MWC361	21 01 36.9	+68 09 48	6.12±0.05	5.58±0.05	4.77±0.05	12/17/2005
MWC1080	23 17 25.6	+60 50 43	7.38±0.05	6.04±0.05	4.68±0.05	12/17/2005

A.2. "Effective Baselines" as a tool in characterizing visibility information on MWC275.

Let $B_{projected}$ be the projected interferometric baseline and let $V(B_{projected})$ be the visibility for a circularly symmetric brightness distribution. For a flat disk inclined at angle ϕ and oriented at some PA, we plotted $V(B_{eff})$ in Fig 5. The effective baseline B_{eff} is defined as -

$$B_{eff} = B_{projected}\sqrt{\cos^2(\theta) + \cos^2(\phi)\sin^2(\theta)}$$

where θ is the angle between the uv vector for the observation and the major axis of the inclined disk and ϕ is the inclination of the disk (0° inclination is face on). Effective baselines account for the decrease in interferometric resolution due to the inclination of the disk in the sky. They capture the geometry of flat disks correctly, but the geometry of finitely thick disks is represented only approximately (optical depth effects and 3-D geometry of thick disks are not taken into account). Here, we argue that effective baselines are good (albeit approximate) tools for capturing details of the MWC275 disk geometry.

In order to determine the inclination angle and sky orientation of the disk, we adopted the following procedure. MC275 visibility values measured with W1W2, S2W2 and E2S2 CHARA-telescope-pairs are close to and just prior to the first minimum in the visibility curve (see Fig 5). In this region the visibility-baseline relation for the emission models in Fig 6 can be approximated with a linear function. We calculated reduced χ^2 values for the best-fit line to the W1W2, S2W2 and E2S2 visibilities as a function of effective baseline, varying the assumed inclination and position angle of the observed disk. Fig 19 shows the reduced χ^2 surface for the fits, plotted against the assumed disk-inclination and position angle. To further illustrate the change in quality of fits as inclination and position angles are varied , Fig 20 shows the linear fits to the visibility vs effective baseline data set.

As seen in Figs 19 and 20, the quality of the fits show dramatic improvement at MWC275 disk PA of $136^o\pm2^o$ and inclination of $48^o\pm2^o$. These values are very close to a disk PA of $139^o\pm15^o$ and inclination of 51^{+11}_{-9} degrees determined in Wassell et al. (2006). The excellent agreement in inclination and PA values for MWC275 from two independent methods strongly supports a disk model for MWC275, validating the use of "effective baselines" to plot MWC275 visibilities.
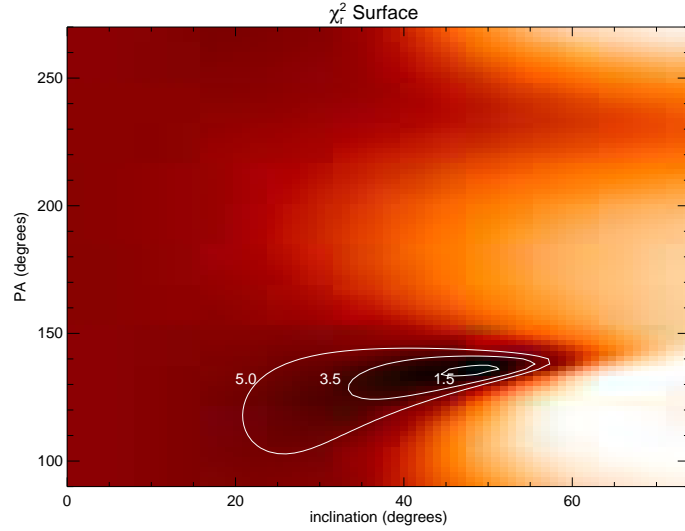
Fig. 19.— Reduced χ^2 surface for the linear fits to the observed visibilities (obtained with the W1W2, S2W2 and E2S2 CHARA-telescope-pairs) as a function of effective interferometric baseline. The solid curves are reduced χ^2 contours of 5, 3.5 and 1.5 respectively.
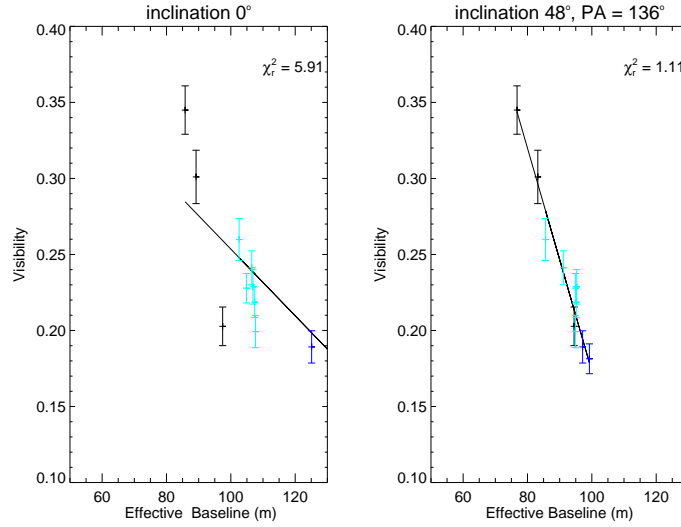

Fig. 20.— Linear fits to the observed visibilities (obtained with the W1W2, S2W2 and E2S2 CHARA-telescope-pairs) as a function of effective interferometric baseline. The data symbols are explained in Fig. 3a.

REFERENCES

Akeson, R. L., Boden, A. F., Monnier, J. D., Millan-Gabet, R., Beichman,C., Beletic, J., Calvet, N., Hartmann, L., Hillenbrand, L., Koresko, C., Sargent, A. & Tannirkulam, A. 2005b ApJ, 635, 1173

Akeson, R. L., Walker, C. H., Wood, K., Eisner, J. A., Scire, E., Penprase, B., Ciardi, D. R., van Belle, G. T., Whitney, B. & Bjorkman, J. E. 2005a, ApJ, 622, 440

Barth, A. J. 2001, ASP Conf. Ser., 238, 385

Berger, D. H., Monnier, J. D., Millan-Gabet, R., ten Brummelaar, T. A., Muirhead, P., Pedretti, E. & Thureau, N. 2006, Proceedings of SPIE, 6268, 62683K

van Boekel, R., Min, M., Leinert, Ch., Waters, L. B. F. M., Richichi, A., Chesneau, O., Dominik, C., Jaffe, W., Dutrey, A., Graser, U., Henning, Th., de Jong, J., Köhler, R., de Koter, A., Lopez, B., Malbet, F., Morel, S., Paresce, F., Perrin, G., Preibisch, Th., Pryzgodda, F., Schöller, M. & Wittkowski, M. 2004, Nature, 432, 479

van Boekel, R., Dullemond, C. P. & Dominik, C. 2005, A&A, 441, 563

van Boekel, R., Min, M., Waters, L. B. F. M., de Koter, A., Dominik, C., van den Ancker, M. E. & Bouwman, J. 2005, A&A, 437, 189

Calvet, N., Magris, G. C., Patino, A. & D'Alessio, P. 1992, Rev. Mex. Astron. Astrofis, 24, 27

Calvet, N., Patino, A., Magris, C. G. & D'Alessio, P. 1991, ApJ, 380, 617

Chiang, E. I., Joung, M. K., Creech-Eakman, M. J., Qi, C., Kessler, J. E., Blake, G. A. & van Dishoeck, E. F. 2001, ApJ, 547, 1077

Chiang, E., I. & Goldreich, P. 1997, ApJ, 490, 368

Corder, S., Eisner, J. & Sargent, A. 2005, ApJ, 622, L133

D'Alessio, P., Calvet, N., Hartmann, L., Franco-Hernandez, R. & Servin, H. 2006, ApJ, 638, 314

D'Alessio, P., Calvet, N. & Hartmann, L. 2001, ApJ, 553, 321

Dominik, C., Dullemond, C. P., Waters, L. B. F. M. & Walch, S. 2003, A&A, 398, 607

Dubrulle, B., Morfill, G., & Sterzik, M. 1995, Icarus, 114, 237

Dullemond, C. P. & Dominik, C. 2004, A&A, 421, 1075

Dullemond, C. P. & Natta, A. 2003, A&A, 408, 161

Dullemond, C. P., Dominik, C. & Natta, A. 2001, ApJ, 560, 957

Eisner, J. A., Lane, B. F., Akeson, R. L., Hillenbrand, L. A. & Sargent, A. I. 2003, ApJ, 588, 360

Eisner, J. A., Lane, B. F., Hillenbrand, L. A., Akeson, R. L. & Sargent, A. I. 2004, ApJ, 613, 1049

Eisner, J. A., Chiang, E. I., Lane, B. F. & Akeson, R. L. 2007a, 657, 347.

Eisner, J. A. 2007b, Nature, 447, 562

Ferguson, J. W., Alexander, D. R., Allard, F., Barman, T. & 4 coauthors 2005, ApJ, 623, 585

Fukagawa, M., Hayashi, M., Tamura, M., Itoh, Y., Hayashi, S. S., Oasa, Y. & 17 co-authors 2004, ApJ, 605, L53

Garcia Lopez, R., Natta, A., Testi, L. & Habart, E. 2006, A&A, 459, 847

Grady, C. A., Woodgate, B., Bruhweiler, F. C., Boggess, A., Plait, P.,Lindler, D. J., Clampin, M. & Kalas, P. 1999, ApJ, 523, L151

Grady, C. A., Devine, D., Woodgate, B., Kimble, R., Bruhweiler, F. C., Boggess, A., Linsky, J. L., Plait, P., Clampin, M. & Kalas, P. 2000,ApJ, 544, 895

Hanner, M. 1988, Grain optical properties, Technical report

Harries, T. J. 2000, MNRAS, 315, 722

Harries, T. J., Monnier, J. D., Symington, N. H. & Kurosawa, R. 2004, MNRAS, 350, 565

Hillenbrand, L. A., Strom, S. E., Vrba, F. J. & Keene, J. 1992, ApJ, 397, 613

Jones, B. & Puetter, R. 1993, Proc. of SPIE, 1946, 610

Kraus, A., Preibisch, T. & Ohnaka, K. 2008, A&A, 676, 490

Kurosawa, R., Harries, T. J., Bate, M. R. & Symington, N. H. 2004, MNRAS, 351, 1134

Kurucz, R. L. 1970, SAO Special Report 308 (Cambridge: SAO)

Isella, A. & Natta, A. 2005, A&A, 438, 899

Isella, A., Testi, L. & Natta, A. 2006, A&A, 451, 951

Isella, A., Natta, A. & Testi, L. 2007, A&A, 469, 213

Kamp, I. & Dullemond, C. P. 2004, ApJ, 615, 991

Kenyon, S. & Hartmann, L. 1987, ApJ, 323, 714

Lamers, H. J. G. L. M. & Waters, L. B. F. M. 1984, A&A, 136, 37

Leinert, Ch., van Boekel, R., Waters, L. B. F. M., Chesneau, O.,Malbet, F. & Khler, R. 2004, A&A, 423, 537

Liu, W. M., Hinz, P. M., Meyer, M. R., Mamajek, E. E., Hoffmann, W. F., Brusa, G., Miller, D.& Kenworthy, M. A. 2007, ApJ, 658, 1164

Lucy, L. B. 1999, A&A, 344, 282

Mannings, V. & Sargent, A. I. 1997, ApJ, 490, 792

Mariñas, N., Telesco, C. M., Fisher, R. S., Packham, C.& Radomski, J. T. 2006, 653, 1353.

Meeus, G., Waters, L. B. F. M., Bouwman, J., van den Ancker, M. E., Waelkens, C. & Malfait, K. 2001, A&A, 365, 476

Merand, A., Borde, P. & Coude Du Foresto, V. 2004, A&A, 433, 1155

Millan-Gabet, R., Schloerb, F. P. & Traub, W. A. 2001, ApJ, 546, 358

Millan-Gabet, R., Schloerb, F. P., Traub, W. A., Malbet, F., Berger, J. P. & Bregman, J. D. 1999, ApJ, 513, L131

Miroshnichenko, A., Ivezic, Z. & Elitzur, E. 1997, ApJ, 475, 41

Monnier, J. D., Tannirkulam, A., Tuthill, P. G., Ireland, M., Cohen, R., Danchi, W. C. & Baron, F. 2008, submitted.

Monnier, J. D., Zhao, M., Pedretti, E., Thureau, N., Ireland, M., Muirhead, P. & 10 coauthors 2007, Science, 317, 5836, 342.

Monnier, J. D., Berger, J. P., Millan-Gabet, R., Traub, W. A., Schloerb, F. P., Pedretti, E., Benisty, M., Carleton, N. P., Haguenauer, P., Kern, P., Labeye, P., Lacasse, M. G., Malbet, F., Perraut, K., Pearlman, M. & Zhao, M. 2006, ApJ, 647, 444

Monnier, J. D., Millan-Gabet, R., Billmeier, R., Akeson, R. L., Wallace, D., Berger, J. P., Calvet, N., D'Alessio, P., Danchi, W. C., Hartmann, L. & 24 coauthors, 2005, ApJ, 624, 832

Monnier, J. D., Tuthill, P. G., Ireland, M. J., Cohen, R. & Tannirkulam, A. 2004, AAS 205, 36, 1367

Monnier, J. D., Principles of LongBaseline Stellar Interferometry, Course notes from the 1999 Michelson Summer School, Edited by P. R. Lawson (JPL Publication) 2000, 9, 203

Monnier, J. D. & Millan-Gabet, R. 2002, ApJ, 579, 694

Muzerolle, J., D'Alessio, P., Calvet, N., & Hartmann, L. 2004, ApJ, 617, 406

Natta, A., Testi, L., Neri, R., Sheperd, D. S. Wilner, D. J. 2004, A&A, 416, 179

Natta, A., Prusti, T., Neri, R., Wooden, D., Grinin, V. P. & Mannings, V. 2001, A&A, 371, 186

Oppenheimer, B. R., Brenner, D., Hinkley, S., Zimmerman, N., Sivaramakrishnan, A. & 7 coauthors 2008, ApJ, 680

Ossenkopf, V., Henning, Th., Mathis, J. S. 1992, A&A, 261, 567

Pinte, C., Menard, F., Berger, J. P., Benisty, M. & Malbet, F. 2008 A&A, in press

Pollack, J. B., Hollenbach, D., Beckwith, S., Simonelli, P. D., Roush, T. & Fong, W. 1994, ApJ, 421, 615

Pontoppidan, K. M., Dullemond, C. P., Blake, G. A., Adwin Boogert, A. C., van Dishoeck, E. F., Evans, N. J., Kessler-Silacci, J. & Lahuis, F. 2007, ApJ, 656, 980.

Rettig, T., Brittain, S., Simon, T., Gibb, E., Balsara, D. S., Tilley, D. A. & Kulesa, C. 2006, ApJ, 646, 342

Landolt, A. U. 1983, A&A, 88, 439

Lin, S., Ohashi, N., Lim, J., Ho, P., Fukagawa, M. & Tamura ,M. 2006, ApJ, 645, 1297

Shakura, N. I. & Sunyaev, R. A. 1973, A&A, 24, 337

Semenov, D., Pavlyuchenkov, Ya., Schreyer, K., Henning, Th., Dullemond, C. & Bacmann, A. 2005, ApJ, 621, 853

Sitko, S. L., Carpenter, W. J., Kimes, R. L., Wilde, J. L., Lynch, D. K., Russel, R. W., Rudy, R. J., Mazuk, S. M., Venturini, C. C., Puetter, R. C., Grady, C. A., Polomski, E. F., Wisnewski, J. P., Brafford, S. M., Hammel, H. B. & Perry, R. B. 2008, ApJ, 678, 1070

ten Brummelaar, T. A., McAlister, H. A., Ridgway, Bagnuolo, W. G. Jr., Turner, N. H., Sturmann, L., Sturmann, J., Berger, D. H., Ogden, C. E., Cadman, R., Hartkopf, W. I., Hopper, C. H. & Shure, M. A., 2005, ApJ, 628, 453

Tannirkulam, A. T., Monnier, T. J., Monnier, J. D., Millan-Gabet, R., Harries, T. J., Pedretti, E., ten Brummelaar, T., McAlister, H., Turner, N., Sturmann, J., & Sturmann, L. 2008, ApJ, submitted

Tannirkulam, A. T., Harries, T. J. & Monnier, J. D. 2007, ApJ, 661, 374

Tuthill, P. G., Monnier, J. D. & Danchi, W. C. 2001, Nature, 409, 1012

Vinkovic, D., Ivezic, Z., Jurkic, T. & Elitzur, M. 2006a, ApJ, 636, 348

Walker, C., Wood, K., Lada, C. J., Robitaille, T., Bjorkman, J. E. & Whitney, B. 2004, MNRAS, 351, 607

Wassell, E. J., Grady, C. A., Woodgate, B., Kimble, R. A. & Bruhweiler, F. C. 2006, ApJ, 650, 985.

Weiner, J., Tatebe, K., Hale, D. D. S., Townes, C. H., Monnier, J. D., Ireland, M., Tuthill, P. G., Cohen, R., Barry, R. K., Rajagopal, J.& Danchi, W. C. 2006, ApJ, 636, 1067

Weingartner, J. C. & Draine, B. T. 2001, ApJ, 548, 296

Wisniewski, J. P., Clampin, M., Grady, C. A, Ardila, D. R., Ford, H. C., Gomilowski, D. A., Illingworth, G. D., & Krist, J. E. 2008, ApJ, accepted

Wood, K., Mathis, J., S. & Ercolano, B. 2004, MNRAS, 348, 1337

Zhu, Z., Hartmann, L., Calvet, N., Hernandez, J., Muzerolle, J., & Tannirkulam, A. 2007, ApJ, 669, 483